https://doi.org/10.5194/egusphere-2025-2909
Preprint. Discussion started: 12 August 2025

On the criticality of return flows in viscous accretionary wedges and its implications for deep-crustal exhumation in subduction zones

Ayan Patsa[1] and Nibir Mandal[1]

[1]Department of Geological Sciences, Jadavpur University, Kolkata 700032, India

Correspondence: Nibir Mandal (nibir.mandal@jadavpuruniversity.in)

Abstract. In subduction zones, the accretionary wedges play a vital role in mediating the burial processes of incoming oceanic sediments and eventually their return pathways to the surface. A direction of the previous tectonic models invoked the standard corner flow theory, assuming a slab-parallel shear and a rigid, fixed overriding plate, to elucidate the crustal recycling processes in tectonic wedges. To deal with more complex subduction-collisional settings, where they have deformable overriding plates, and associate a horizontal slab migration (advance or rollback) component during subduction, we develop a generalized corner flow model to revisit the problem of return flow mechanics, providing a criticality analysis of the return flows as a function of the geometric, kinematic, and rheological conditions in accretionary wedges. A new set of analytical solutions is presented to evaluate the limiting conditions in which a wedge can set in significant return flows, leading to focused exhumation of the deep-crustal materials. The theoretical results suggest that, for moderate wedge-taper angles (~30^o), the viscosity ratios (μ_r) between the overriding plate and the wedge $\geq$ ~10^3 provide favourable tectonic settings for the return flow kinematics in accretionary wedges. Decrease in μ_r, or addition of slab roll back weakens the return flows, whereas slab advance greatly strengthens the return flows. The analytical solutions are also utilized to demonstrate reversals in the shear-sense patterns across the wedge. We expand this study by reproducing some of the theoretical flow patterns in laboratory experiments. It is shown from the theoretical model that the total pressure in the accretionary wedge dynamics becomes close to the lithostatic value when the rheological setting has low-viscosity (10^{19} Pa s) wedge materials.

1 Introduction

Accretionary wedges that generally accommodate large volumes of sediments fed by subducting oceanic plates play a critical role in modulating the mechanics of active plate interfaces in subduction zones (Agard et al., 2018; Angiboust et al., 2022; Beaumont et al., 1999; Cawood et al., 2009; Cloos and Shreve, 1988). The accreted sediments act as lubricating agents in weakening the plate interface and facilitate the subduction processes (Behr et al., 2022; Behr and Becker, 2018; Hu et al., 2021; Lamb and Davis, 2003; Pusok et al., 2022). Geophysical observations suggest that a fraction of the wedge sediments can also be dragged to deeper mantle regions along the subducting slab in the form of a narrow channel, called subduction channel (Agard et al., 2009; Gerya et al., 2002; Shreve and Cloos, 1986). Petrological investigations reveal the omnipresence of high- and ultra-high-pressure (HP-UHP) and low-temperature (LT) metamorphic rocks preferentially in the accretionary belts of both paleo- and modern subduction zones (Agard et al., 2001; Glodny et al., 2005; Platt, 1993; Warren, 2013). The

https://doi.org/10.5194/egusphere-2025-2909
Preprint. Discussion started: 12 August 2025

metamorphic evolution of HP–LT rocks thus provide key information about the deep-crustal tectonic processes, beginning from burial of sediments and shallow-crustal materials, followed by their HP metamorphism at greater depths and finally their exhumation back to Earth's surface in course of the convergence movements (Van Dinther et al., 2012; Yamato et al., 2007).During this recycling process, the wedge materials also undergo syn-metamorphic deformations in multiple episodes, giving rise to complex tectonic structures at convergent plate boundaries (Allemand and Lardeaux, 1997; Ring et al., 2020). Understanding the kinematics of accretionary wedges is thus crucially important to interpret the mechanisms of deep-crustal exhumations and associated tectonic processes in subduction zones, which is the central theme of the present theoretical study.

Geochemical and geochronological records of exhumed blueschists and eclogites suggest that high-pressure rocks can be exhumed at varied rates (< 1 mm/yr to a few cm/yr) depending upon the tectonic environments (Agard et al., 2009; Ernst et al., 1988; Rubatto and Hermann, 2001). Conceptual, analytical and numerical models consider a wide range of factors, such as erosion and isostatic adjustment (Brandon et al., 1998; England and Richardson, 1977), buoyant flow of low density crustal units (Chemenda et al., 1995; Ernst et al., 1997), corner flow circulation within accretionary wedges (Burov and Yamato, 2008; Cloos, 1982; Moulas et al., 2021), extension-driven ductile thinning and normal faulting (Platt, 1986; Ring and Brandon, 2008), among others (see Platt (1993); **?**, for review) to account for such variations in the exhumation rates. Among them, the corner flow (CF) model (Batchelor, 1967), which was implemented by Cloos (1982), deals with the problem of exotic high-pressure/low-temperature (HP/LT) blocks within a mudstone matrix in the Franciscan Complex of California. According to this tectonic model, the crustal materials in the lower part of the wedge are dragged down with the subducting plate, eventually set to reverse their flow directions, as illustrated in Fig. 1. This reversal of flow, hereafter called *return flow*, causes syn-subduction exhumation of deep-crustal rocks back to the surface. The corner flow mechanism successfully explains the coherent occurrence of extensive HP metamorphic belts with progressively increasing P-T conditions. Petrological data syntheses (e.g., Agard et al. (2001)) point to, at least two different corner-flow circulations in the tectonic evolution of HP and UHP metamorphic complexes: a relatively shallower (up to 40 km) circulation within accretionary complexes that can be correlated with the formation and exhumation of blueschists and most eclogites, and a deeper circulation in subduction channels, which is responsible for the formation and exhumation of UHP eclogites (Agard et al., 2009; Burov et al., 2001; Wang et al., 2019).

The return flow kinematics has been extensively used in analytical studies of viscous flows in narrow (subduction channel) and wide (accretionary wedge) corner regions at the convergence between two rigid or deformable plates (Cloos, 1982; Grujic, 2006; Iwamori, 2003; Mancktelow, 1995; Moulas et al., 2021). Numerical CF models, including both fixed and evolving corner geometry produce return flows in accretionary wedges and subduction channels (Allemand and Lardeaux, 1997; Angiboust et al., 2022; Gerya et al., 2002; Yamato et al., 2007; Beaumont et al., 2009; Sanhueza et al., 2022). These models impose subduction-related velocity boundary conditions either at the walls of the wedge or at the boundaries of a large model box. Some of them (e.g. Van Dinther et al. (2012)) also allow subduction to be dynamically driven by the slab pull force. Interestingly, some models do not produce the classical corner flow kinematics within the accretionary wedges (see Candioti et al. (2021); Pusok et al. (2022)). In addition, the exhumation velocities obtained from dynamic CF models (Van Dinther et al., 2012; Yamato et al., 2007) are comparable to those estimated from radiometric dating of exhumed continuous HP units (Agard et al., 2002; Federico et al., 2005), but low compared to those obtained in the earlier analytical and some numerical models

https://doi.org/10.5194/egusphere-2025-2909
Preprint. Discussion started: 12 August 2025

(Allemand and Lardeaux, 1997; Cloos, 1982; Marques et al., 2018). These contrasting findings lead to a few fundamental questions on the mechanics of the return flows: (1) what are the factors in modulating weak versus strong return flows, (2) what controls the exhumation rates of the returning wedge materials, and (3) how does the varying flow kinematics affect the deformation patterns within the wedge as well as the overriding plate? These questions motivate this theoretical study to explore the conditions that facilitate the return flows kinematics and associated deformations in the deeper, viscously deforming part of accretionary wedges (Fernández-Blanco et al., 2020; Pavlis and Bruhn, 1983).

Recent lithospheric-scale, self-organizing, and rheologically advanced thermo-mechanical models, as implemented in e.g., Burov et al. (2001); Li et al. (2010); Van Dinther et al. (2012); Yamato et al. (2007), have extensively dealt with the long-term dynamic evolution of the wedge geometry and kinematics. However, analytical models, in spite of their several simplifications, are effective in evaluating the system through given boundary conditions and parameters, without losing the perspective of the natural prototype. Although the classical CF model of Cloos (1982) provides an analytical solution for the velocity field in a corner region, the solution is applicable to a setting with the boundary velocity parallel to the channel's base, and that too for a fixed and rigid hanging wall of the channel. Subduction zones, however, often evolve through slab rollback or slab advance (Bezada et al., 2013; Cawood et al., 2009; Di Giuseppe et al., 2009; Nakakuki and Mura, 2013), which originate from a complex interplay of various forces, such as, ridge push, slab pull, and mantle convection (Ribe, 2010; Schellart, 2008; Xue et al., 2022). In such cases, the instantaneous subduction velocity vector operates oblique to the slab and bottom boundary of the wedge. Additional kinematic complexities occur also due to significant deformations in the overriding plate, implying that the assumption of rigid hanging wall in the CF solution may not always be geologically tenable (Schellart, 2024).

In this article, we develop a modified corner flow solution, incorporating the effect of slab-oblique subduction on the flow kinematics in an accretionary wedge with a deformable hanging wall. Our modelling approach is simple in the fact that it assumes an already existing homogeneous, linear viscous wedge above the subducting plate and overviews the complex processes in the accretionary wedge (Angiboust et al., 2022; Clift and Vannucchi, 2004; Simpson, 2010). Such simplifications provide a quantitative analysis of the various parameters controlling the first order kinematics of a mature, steady-state wedge (Yamato et al., 2007). The parametric analysis presents the individual effects of obliquity of subduction, wedge geometry (narrow vs. wide), viscosity of the wedge as well as the overriding plate, and an imposed overriding plate velocity on the flow and deformation pattern within the accretionary wedge. The CF solution, supported by physical laboratory experiments, allows us to decipher the specific conditions required for return flows (and hence exhumation) of deep-crustal materials in an accretionary wedge. Finally, we utilize the CF model to examine the possibilities of significant non-lithostatic pressure developments within the wedge, as reported in some previous studies (e.g., Gerya (2015); Mancktelow (1995); Raimbourg and Kimura (2008)).

https://doi.org/10.5194/egusphere-2025-2909
Preprint. Discussion started: 12 August 2025

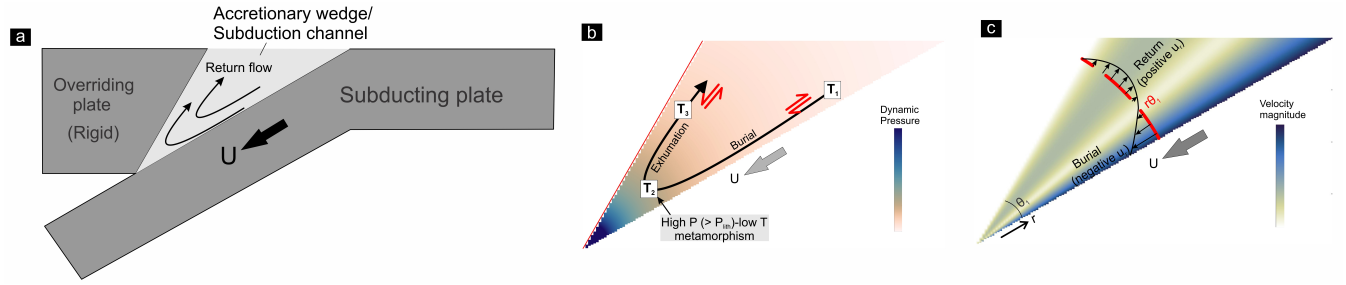

Figure 1. (a) A schematic presentation of the return flow pattern in accretionary wedges/ subduction channels. U: subduction velocity. (b) Particle paths in the ideal corner flow within a wedge. The particles undergo the following sequential events: 1) burial in the time interval between T_1 and T_2; 2) high P- low T metamorphism at T_2, where the total pressure (P) exceeds the lithostatic pressure (P_{lith}), and finally, 3) return flow-driven exhumation in the time interval between T_2 to T_3. Note that the wedge develops opposite shear senses in the lower and upper parts. (c) Velocity profile across the wedge. Negative and positive values of the radial velocity component (u_r) indicate burial and exhumation, respectively. θ_1: wedge taper angle. r: distance from the wedge tip.

2 Theory

2.1 Basic premises

The present theoretical model is developed in the premises of downward-tapering accretionary wedges, which has been extensively used in earlier theoretical models (Cloos, 1982), analogue experiments (Luján et al., 2010) and numerical simulations (Pusok et al., 2022; Yamato et al., 2007). To simplify the theoretical treatment, the wedge is assumed to terminate at a fixed-point S, located at a depth of about 40 km (S-point boundary condition of Willett et al. (1993)) (Fig. 2a). However, the wedges in subduction zones can describe a narrow opening at their base, allowing a small fraction of the sediments to be transported into mantle depths (Agard et al., 2009). Traditionally, researchers have modelled accretionary wedges using Coulomb materials, primarily to analyze their mechanical stability as a function of the taper angle (Dahlen et al., 1984; Dahlen, 1990). This modelling approach is, however, applicable for shallow-crustal deformations. Below the brittle-ductile transition, at middle and lower crustal depths, viscous processes dominate in the wedge deformations (Mannu et al., 2016; Pavlis and Bruhn, 1983), and thereby demand a viscous rheological approach. To capture the exclusive effects of viscous wedge kinematics, our theoretical treatment excludes the additional influence of gravity that can arise due to the density contrast between the wedge and the overriding plate, especially at low subduction velocities (Ernst et al., 1997; Maiti et al., 2020; Beaumont et al., 2009). We consider Newtonian viscous rheology to develop the present theoretical model. The choice of linear rheology for the wedge is simplification of the nature considering that rocks often behave as a power-law fluid (Ranalli, 1995). However, it has been shown previously that the non-linearity of the rheology plays little role in the first-order kinematics of a corner flow (Ribe, 2015, 2018).

In the CF model of Cloos (1982), the upper bounding plate of the wedge (i.e., the overriding plate, hereafter abbreviated as OP) is considered rigid and held fixed, and the lower bounding plate (i.e., the subducting plate, hereafter abbreviated as SP)

https://doi.org/10.5194/egusphere-2025-2909
Preprint. Discussion started: 12 August 2025

moves downward with the velocity vector oriented parallel to the wedge boundary (Fig. 1a). However, the OPs, especially the young and hot ones, can accommodate large deformations with the accretionary wedges in subduction settings. In addition, the subducting slab movements can occur oblique to the wedge-slab interface when the convergent settings experience slab advance or rollback. To overcome the model limitations of Cloos (1982), Moulas et al. (2021), advanced the approach for a deformable OP setting, showing that the flow patterns in subduction channels differ significantly from those obtained from the rigid overriding plate model, especially when the viscosity ratios between the OP and the wedge materials are low. In this article, we generalize the theory of Moulas et al. (2021) incorporating slab-oblique kinematic conditions. The subducting slab movements towards the OP and the ocean are considered to represent the slab advance and slab rollback kinematics, respectively. We simplify our theoretical approach assuming that the slab undergoes translational motion without any along slab gradient of the linear subduction vector. Our model also only considers the flow in the vertical plane perpendicular to the trench, and does not consider any trench-parallel flow in the wedge.

2.1.1 Rigid overriding plate model

The 2D accretionary wedge model is represented by a triangular domain of linearly viscous (μ_1) materials, sandwiched between a SP and an OP. The wedge walls converge to each other downward, forming a taper angle θ_1 (Fig. 2a, b). The rigid OP is held fixed. The SP moves at a velocity U, obliquely to the wedge base at an angle ϕ (positive anticlockwise; Fig. 2a, b). The slab-parallel component of U is the subduction velocity, U_s, and its horizontal component represents the slab migration velocity, U_m. In the following discussions, we use the term *subduction obliquity* to define the angle ϕ, measured in the trench-perpendicular vertical plane, which is different from the term generally used to describe the angular relationship of the convergence velocity vector with the trench line in the horizontal plane (McCaffrey, 1992). Positive and negative values of ϕ represent slab rollback and advance, respectively in this theoretical treatment. We consider no-slip boundary conditions at the two wedge walls, and also assume that the wedge undergoes no volume loss or material accretion during the deformation. A Cartesian frame *xy* is chosen with origin at the S-point of the wedge, with the *x* and *y* axes oriented in horizontal and vertical directions, respectively, as shown in Fig. 2b. The SP dips at angle α with respect to the horizontal surface. Considering our focus on the flow field in a triangular region, we choose a polar coordinate system for the theoretical analysis, similar to previous CF studies (Cloos, 1982; Moulas et al., 2021). The origin of the coordinate frame is set at the S-point, where *r* and θ represent the distance from the wedge tip (S-point) and the angular distance (positive anticlockwise) measured from the bottom wedge boundary respectively. The instantaneous velocity field within the wedge can be expressed in terms of polar coordinates (*r*, θ) as:

$$u_r = \frac{1}{r}\frac{\partial \psi}{\partial \theta} \tag{1a}$$

$$u_\theta = -\frac{\partial \psi}{\partial r} \tag{1b}$$

where u_r and u_θ are the radial and tangential velocity components, respectively and ψ is the stream function. Assuming negligible inertial forces and mass conservation, the stream function ψ for a 2D viscous flow satisfies the biharmonic equation:

https://doi.org/10.5194/egusphere-2025-2909
Preprint. Discussion started: 12 August 2025

$$\nabla^2\left(\nabla^2\psi\right) = 0 \tag{2}$$

Applying the boundary conditions in the present problem, we obtain the following relations:

$$u_r = \frac{1}{r}\frac{\partial\psi}{\partial\theta} = -U\cos\phi, u_\theta = -\frac{\partial\psi}{\partial r} = -U\sin\phi \; at \; \theta = 0 \tag{3}$$

$$u_r = \frac{1}{r}\frac{\partial\psi}{\partial\theta} = 0, u_\theta = -\frac{\partial\psi}{\partial r} = 0 \; at \; \theta = \theta_1 \tag{4}$$

These boundary conditions require that ψ is proportional to *r* everywhere in the wedge domain, including its boundaries. The stream function can be thus expressed as,

$$\psi(r,\theta) = rf(\theta) \tag{5}$$

Substituting ψ in Eq. (2), we find:

$$\nabla^2\left[\frac{1}{r}\left(f + f''\right)\right] = \frac{1}{r^3}\left(f + 2f'' + f^{iv}\right) = 0 \tag{6}$$

where the primes denote the order of differentiation on *f*. The solution of Eq. (6) follows:

$$f(\theta) = Asin\theta + Bcos\theta + C\theta sin\theta + D\theta cos\theta \tag{7}$$

where *A*, *B*, *C* and *D* are four constants, which need be solved using four equations. Substituting f in Eq. (5) and putting the derivative expression in Eq. (1) we get:

$$u_r = Acos\theta - Bsin\theta + C\left(sin\theta + \theta cos\theta\right) + D\left(cos\theta - \theta sin\theta\right) \tag{8a}$$

$$u_\theta = -\left(Asin\theta + Bcos\theta + C\theta sin\theta + D\theta cos\theta\right) \tag{8b}$$

Putting θ = 0, and θ_1 in Eq. (8) and comparing the resulting expression with the boundary conditions of Eqs. (3), and (4), it follows

$$A + D = -U\cos\phi \tag{9a}$$

$$B = U\sin\phi \tag{9b}$$

$$Acos\theta_1 - Bsin\theta_1 + C\left(sin\theta_1 + \theta_1 cos\theta_1\right) + D\left(cos\theta_1 - \theta_1 sin\theta_1\right) = 0 \tag{9c}$$

$$Asin\theta_1 + Bcos\theta_1 + C\theta_1 sin\theta_1 + D\theta_1 cos\theta_1 = 0 \tag{9d}$$

https://doi.org/10.5194/egusphere-2025-2909
Preprint. Discussion started: 12 August 2025

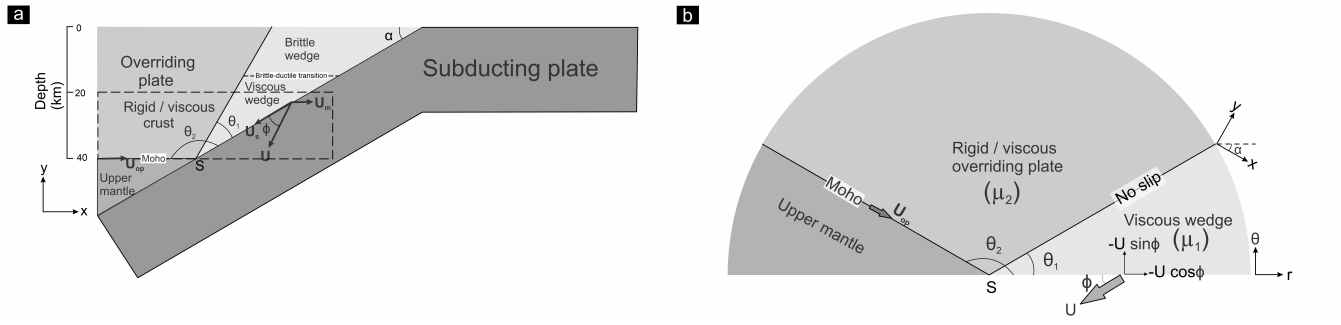

Figure 2. (a) Schematic diagram of the tectonic setting considered for the present theoretical treatment. The subducting plate, dipping at angle α, moves downward obliquely at an angle ϕ to the bottom boundary of the wedge. Dashed rectangle demarcates the region of interest in this study. (b) Theoretical model setup in polar coordinate system (r, θ). The wedge and the overriding plate describe taper angles of θ_1 and ($\theta_2 - \theta_1$), respectively. μ_1: wedge material viscosity. The overriding plate is considered either rigid or deformable (viscosity μ_2). See text for details.

The solutions of Eq. (9) are:

$$A = \frac{U}{(\theta_1^2 - \sin^2\theta_1)} \left[sin\phi\,(\theta_1 + sin\theta_1 cos\theta_1) - \theta_1^2 cos\phi\right) \tag{10a}$$

$$B = U\sin\phi \tag{10b}$$

$$C = \frac{U}{(\theta_1^2 - \sin^2\theta_1)} [cos\phi\,(\theta_1 - sin\theta_1 cos\theta_1) - sin\phi\sin^2\theta_1] \tag{10c}$$

$$D = \frac{U}{(\theta_1^2 - \sin^2\theta_1)} [-sin\phi\,(\theta_1 + sin\theta_1 cos\theta_1) + cos\phi\sin^2\theta_1] \tag{10d}$$

2.1.2 Deformable overriding plate model

To deal with the kinematic problem of accretionary wedges with deformable OP, we solve the velocity field in two corner regions (Anderson and Davis, 1993; Moulas et al., 2021) representing the wedge and the overriding plate (Fig. 2b). The theoretical model setup is considered same as in the rigid OP model, except that the present case incorporates an additional corner region with viscosity μ_2 in the hanging wall of the wedge, representing the viscous crust of the overriding plate (Moulas et al., 2021). The OP - wedge viscosity ratio is denoted as μ_r (= μ_2/μ_1). The wedge and the overriding plate have taper angles θ_1 and $\theta_2 - \theta_1$ respectively. In this analysis, we also impose a velocity (U_{op}) at the Moho of the overriding plate. Several authors have, however, argued that the cold upper mantle beneath the OP in proximity to the subduction zone is stationary and does not participate in the surrounding mantle corner flow (Lee and Kim, 2023; van Keken and Wilson, 2023). The presence of this cold region is attributed to mechanical decoupling at the interface between the forearc mantle and subducting slab (Abers et al., 2017; Wada et al., 2009). Hence, in most of our theoretical analyses, we consider U_{op} to be equal to zero.

https://doi.org/10.5194/egusphere-2025-2909
Preprint. Discussion started: 12 August 2025

We choose two stream functions: ψ_1 and ψ_2 for solving the velocity fields in the wedge and the OP crustal domains, respectively. Similar to the theoretical treatment in section 2.2.1, the two stream functions are expressed in the form:

$$\psi_1(r,\theta) = r f_1(\theta) \tag{11a}$$

$$\psi_2(r,\theta) = r f_2(\theta) \tag{11b}$$

where,

$$f_1(\theta) = A_1 sin\theta + B_1 cos\theta + C_1 \theta sin\theta + D_1 \theta cos\theta \tag{12a}$$

$$f_2(\theta) = A_2 sin\theta + B_2 cos\theta + C_2 \theta sin\theta + D_2 \theta cos\theta \tag{12b}$$

A_i, B_i, C_i, D_i (i = 1, 2) represent eight constants. To find the velocity fields in the wedge and OP regions, we need to evaluate the eight constants, which evidently demands eight boundary conditions. At the subducting plate-wedge interface, the two velocity boundary conditions in terms of polar coordinates (r, θ) is:

$$(u_r)_{\theta = 0} = -U\cos\phi \tag{13a}$$

$$(u_\theta)_{\theta = 0} = -U\sin\phi \tag{13b}$$

$$(u_r)_{\theta = \theta_2} = -U_{op} \tag{14a}$$

$$(u_\theta)_{\theta = \theta_2} = 0 \tag{14b}$$

Assuming no slip at the wedge - OP interface, the velocity continuity across this interface leads to:

$$((u_r)_{\theta = \theta_1})_{wd} = ((u_r)_{\theta = \theta_1})_{op} \tag{15a}$$

$$((u_\theta)_{\theta = \theta_1})_{wd} = ((u_\theta)_{\theta = \theta_1})_{op} \tag{15b}$$

where the subscripts *wd* and *op* refer to the wedge and the overriding plate. The total normal stress as well as the shear stress must be continuous across the wedge - OP interface. The deviatoric stress tensor τ_{ij} is expressed in polar coordinates (r, θ) as,

$$\begin{bmatrix} \tau_{rr} & \tau_{r\theta} \\ \tau_{\theta r} & \tau_{\theta\theta} \end{bmatrix} = \begin{bmatrix} 2\mu_i \frac{\partial u_r}{\partial r} & \mu_i \left(\frac{1}{r}\frac{\partial u_r}{\delta\theta} + \frac{\partial u_\theta}{\delta r} - \frac{u_\theta}{r}\right) \\ \mu_i \left(\frac{1}{r}\frac{\partial u_r}{\partial\theta} + \frac{\partial u_\theta}{\partial r} - \frac{u_\theta}{r}\right) & 2\mu_i \left(\frac{1}{r}\frac{\partial u_\theta}{\partial\theta} + \frac{u_r}{r}\right) \end{bmatrix} \tag{16}$$

where μ_i (i =1, 2) denotes the viscosities of the two corner regions. The total stress tensor σ_{ij} is given by:

$$\sigma_{ij} = -P\delta_{ij} + \tau_{ij} \tag{17}$$

where P is the total pressure, given by the sum of static pressure (P_s) and dynamic pressure (P_d). As P_s has no implications in the present corner flow solution, $P = P_d$, which can be determined from the stress-equilibrium equation,

$$-\frac{\partial P_d}{\partial r} + \frac{1}{r}\frac{\partial \tau_{r\theta}}{\partial\theta} = 0 \tag{18}$$

https://doi.org/10.5194/egusphere-2025-2909
Preprint. Discussion started: 12 August 2025

in the radial direction. Using the boundary condition $P_d = P_0$ at $r = \infty$, we find the integration constant, which appears after solving the differential equation in Eq. (18). P_0 is set as 0 in the given problem, assuming that the dynamic pressure becomes zero at infinite distance away from the S-point of the wedge. The choice of P_0, however, does not qualitatively change the velocity or strain fields either in the wedge or the overriding plate.

The normal components (τ_{rr} and $\tau_{\theta\theta}$) of the deviatoric stress tensor (Eq. 16) in the present setting are zero as there is no extension along as well as across the radial direction, i.e., $\dot{\varepsilon}_{rr} = \dot{\varepsilon}_{\theta\theta} = 0$. This wedge kinematics results because the velocity components at any point (r, θ) within the wedge are independent to r and hence, the radial directions are the directions of the flow apophyse across the wedge. Consequently, the total normal stress (eqn. 17) perpendicular to the wedge-overriding plate interface equals the dynamic pressure P_d. The stress continuity across the interface requires,

$$\left((P_d)_{\theta=\theta_1}\right)_{wd} = \left((P_d)_{\theta=\theta_1}\right)_{op}, \left((\tau_{r\theta})_{\theta=\theta_1}\right)_{wd} = \left((\tau_{r\theta})_{\theta=\theta_1}\right)_{op} \tag{19}$$

Equations (13), (14), (15) and (19) provide the eight boundary conditions, which are utilized to solve the eight unknown constants in Eqn. (12). Their expressions are provided in the Appendix A. Using these constants we determine the two stream functions (ψ_1 and ψ_2) and find the velocity fields in the polar coordinates (r, θ) at the two corner regions from Equation (1) . It is noteworthy that for given U and U_{op}, the velocity field is dependent to θ_1, ϕ, θ_2 (= 180° - α), and μ_r (= μ_1/μ_2) in an accretionary wedge with deformable OP (see Eqs. (A6)-(A13) in Appendix A). This is in contrast to the case with rigid and fixed OP, where the velocity field is entirely dependent on the first two of the aforementioned factors, as discussed in section 2.1. The velocity components determined in the polar coordinate system is converted to the Cartesian frame xy using the following transformation:

$$\begin{bmatrix} u \\ v \end{bmatrix} = \begin{bmatrix} cos\alpha & -sin\alpha \\ sin\alpha & cos\alpha \end{bmatrix} \begin{bmatrix} cos\theta & -sin\theta \\ sin\theta & cos\theta \end{bmatrix} \begin{bmatrix} u_r \\ u_\theta \end{bmatrix} \tag{20}$$

3 Theoretical results

According the CF model (Cloos, 1982; Shreve and Cloos, 1986), the SP movement induces a shear-driven drag in the basal part of the wedge, forcing the wedge materials to flow towards deeper regions. However, the wedge develops dynamic pressures at the tapering end (Fig. 1b). Previous studies have shown that the magnitude of such dynamic pressures can be as high as that of the lithostatic pressure, leading to a condition of tectonic overpressure (Li et al., 2010; Mancktelow, 1995; Marques et al., 2018). The dynamic pressure eventually 'turns' the wedge materials to flow in the reverse directions (*return flows*) towards the surface along the wedge roof (Gerya et al., 2002; Moulas et al., 2021). This flow pattern causes reversal in the vorticity sense across the wedge, where the upper region develops a distinct zone of normal-sense of shear (Fig. 1b). The flow kinematics within the wedge can be decomposed into two parts: 1) shear-driven Couette flows, which result in burial of sediments, and ii) pressure-driven Poiseuille flows, which contribute to exhumation of deep-crustal materials (Fig. 1c).

Return flow in a downward-tapering wedge is considered to be one of the most effective exhumation mechanisms to explain the high P- and low T rock assemblages in the accretionary wedges or subduction channels (Agard et al., 2009; Cloos and

https://doi.org/10.5194/egusphere-2025-2909
Preprint. Discussion started: 12 August 2025

Shreve, 1988; Yamato et al., 2007). For a quantitative analysis of the return flows in a wedge, we introduce a non-dimensional parameter, termed as *return flux* (F_R), which is defined as the ratio of the volumetric rate of materials being returned to that of materials undergoing burial at an instant within the wedge. In the polar coordinate system under consideration, positive and negative values of the radial component (u_r) of the velocity vector indicate the rates of return and burial of wedge materials, respectively (Fig. 1c). For the present simplified 2D problem, we assume the velocity field remaining uniform along the trench, and express F_R as:

$$\mathrm{F}_R = \frac{volumetric\ rate\ of\ return}{volumetric\ rate\ of\ burial} = \frac{\sum_i^{N_1} (positive\ u_r)_i}{\left|\sum_i^{N_2} (negative\ u_r)_i\right|} \tag{21}$$

where N_1 and N_2 represent number of areal elements of regions with positive and negative radial velocity (u_r). High F_R implies a condition of strong return flows (hence exhumation), whereas zero or low F_R indicates either no return flows or a kinematic condition in which the return flows are deflected towards the overriding plate (for deformable overriding plate). The infinitesimal strain field at a point inside the wedge or the OP can be expressed by a stretching-rate tensor (Means et al., 1980) in polar coordinates (r, θ) as:

$$\begin{bmatrix} \dot{\varepsilon}_{rr} & \dot{\varepsilon}_{r\theta} \\ \dot{\varepsilon}_{\theta r} & \dot{\varepsilon}_{\theta\theta} \end{bmatrix} = \begin{bmatrix} \frac{\delta u_r}{\delta r} & \frac{1}{2}\left(\frac{1}{r}\frac{\delta u_r}{\delta\theta} + \frac{\delta u_\theta}{\delta r} - \frac{u_\theta}{r}\right) \\ \frac{1}{2}\left(\frac{1}{r}\frac{\delta u_r}{\delta\theta} + \frac{\delta u_\theta}{\delta r} - \frac{u_\theta}{r}\right) & \frac{1}{r}\frac{\delta u_\theta}{\delta\theta} + \frac{u_r}{r} \end{bmatrix} \tag{22}$$

The eigenvalues and eigenvectors of the stretching-rate matrix (Eqn. (22)) give the values and the orientations of maximum and minimum instantaneous stretching axes, ISA_{max} and ISA_{min} respectively. The vorticity w in polar coordinates (r, θ) can be written as:

$$w = \frac{1}{r}\left[\frac{\delta(ru_\theta)}{\delta r} - \frac{\delta u_r}{\delta\theta}\right] = \frac{2(D\ sin\theta - \mathrm{C}\cos\theta)}{r} \tag{23}$$

For wedges with deformable OPs, the vorticity in the wedge and the OP is determined by replacing C, D of Eqn. (18) by C_1, D_1 and C_2, D_2 respectively. Eqn. (18) shows that the vorticity is inversely proportional to the distance from the tip of the wedge. For our analysis, the vorticity at any point (r, θ) is normalized by the factor $U/(r\theta_1)$. Positive and negative values of the normalized vorticity parameter ($\dot{w}$) indicate anticlockwise and clockwise rotation, respectively. As mentioned in the preceding section 2.2.2, the wedge kinematics and that in the overriding plate depend on several factors (e.g., ϕ, μ_r). We, however, present a parametric analysis to show the impact of the most influential factors in controlling the velocity and strain fields in the wedge. Unless mentioned otherwise, we discuss in the foregoing sections the results for the case of accretionary wedges with a taper angle of 30° and viscosity of 10^{19} Pa s, keeping the OP fixed (i.e., $U_{op} = 0$). In our models the subduction has a dip of 30°, and the SP moves at velocity of 3 cm/yr. The present analysis covers a depth range between 20 km and 40 km (Fig. 2a).

3.1 Parametric analysis

3.1.1 Role of subduction obliquity

Accretionary wedges with SP movements parallel to the basal wedge boundary ($\phi = 0°$) against a fixed rigid OPs localize return flows close to the upper boundary (Fig. 3a-i). F_R calculated from Eq. 21 is 0.97, implying that the crustal materials undergoing

https://doi.org/10.5194/egusphere-2025-2909
Preprint. Discussion started: 12 August 2025

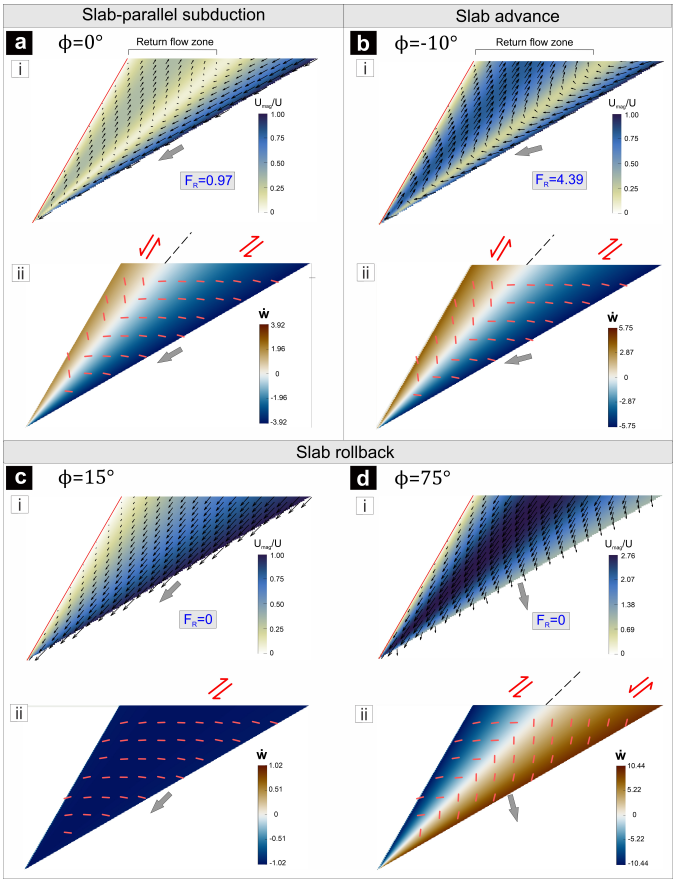

Figure 3. Velocity and vorticity fields within wedges with rigid walls in tectonic settings with varying subduction obliquities (ϕ). θ_1 = 30°, and α = 30°. U_{mag}: flow velocity magnitude and $\dot{w}$: a normalized vorticity parameter. Short red lines mark the orientations of the minimum instantaneous stretching axes (ISA_{min}). Note that addition of a slab advance component substantially multiplies the return flux (F_R), whereas slab rollback lowers F_R.

burial are potentially recycled back to the surface almost in the same quantities at any instant. The analytical solutions indicate that the degree of subduction obliquity strongly controls the flow patterns in wedges. Slab advance kinematics (i.e., negative ϕ) greatly facilitates the return flux, e.g., F_R = 4.39 when ϕ = -10°. The wedge materials extrude at high velocities (∼U) along the inclined wedge roof (Fig. 3b-i), and may even locally exceed the subduction velocity for high negative ϕ (< ∼-15°). In contrast, the slab rollback kinematics (i.e., ϕ is positive) significantly reduces F_R , dropping to zero. This finding suggest that a wedge can fail to produce return flows, unless the rollback velocity is extremely low ($\phi < \sim\theta_1/3$). At higher rollback velocities, all the wedge materials are buried at high velocities, which locally exceed the subduction velocity (Fig. 3c-i, d-i).

The subduction obliquity also controls the viscous strain distributions in the wedge beneath a rigid OP. When ϕ has negative, zero or extremely low positive values ($\phi < \sim\theta_1/3$), the wedge flows show a vorticity sense reversal, from negative (dextral, thrust-sense shear) in the basal part to positive (sinistral, normal-sense shear) in the roof. The upper part of the wedge is

https://doi.org/10.5194/egusphere-2025-2909
Preprint. Discussion started: 12 August 2025

characterized by vertical to sub-vertical ISA_{min} axes (Fig. 3a-ii, b-ii). The field of normal-sense shear in the roof region progressively shrinks with increasing ϕ and becomes insignificant for high slab rollback velocities, corresponding to $\phi > \sim\theta_1/3$. For a relatively large ϕ value ($> \sim 2\theta_1/3$), the basal part of the wedge produces sinistral shear with sub-vertical ISA_{min} axes (Fig. 3d-ii). Conditions in the range $\sim\theta_1/3 < \phi < \sim 2\theta_1/3$, in contrast, produces thrust-sense of shear in the entire wedge domain (Fig. 3c-ii).

3.1.2 Control of overriding plate/wedge viscosity ratio

Our analytical solutions indicate that, in case of a deformable OP, the viscosity ratio, μ_r can strongly influence the flow pattern in the wedge. $\mu_r \geq 10^3$ yields the first order flow pattern similar to that observed in the rigid OP setting. For μ_r = 10^3, the ϕ = 0° subduction condition gives rise to a high return flux (F_R = 0.66), which is, however, less than that (F_R = 0.97) in the equivalent rigid OP setting (Fig. 4a-i). Negative ϕ leads to a condition of exceptionally strong return flux (e.g., F_R = 3.32 when ϕ = -10°), where the return flows attain high velocities (0.7U), comparable to the subduction rates (Fig. 5a-i). However, lower μ_r ($< \sim 10^3$) weakens the confinement of viscous flows within the wedge, allowing the flows to become distributed in the OP region. In such conditions, the materials lying beneath the wedge-roof flow towards the overriding plate, instead of returning back towards the surface (Fig. 4b-i, c-i, 5d-i). This kinematic transformation results in significant weakening of the return flux within the wedge. For ϕ = 0° and -10°, a decrease in μ_r from 10^3 to 10^2 drastically reduces F_R from 0.66 to 0.06, and 3.32 to 0.55, respectively. At μ_r = 10, the wedge hardly develops any return flux (Fig. 4c-i). For considerable slab rollback velocity (positive ϕ), similar to the case with rigid overriding plate, F_R drops to zero for all the viscosity ratios (Fig. 5b-i, c-i, e-i, f-i). The slab rollback process facilitates the burial rates of wedge materials, which may locally exceed the subduction velocity. The condition of relatively low μ_r ($< \sim 10^3$) sets in trench-ward movement of the overriding plate during the slab rollback (Fig. 5e-i, f-i).

In a mechanical condition with μ_r = 10^3, negative, zero or small positive ϕ values result in reversal of shear across the wedge, showing a transition from thrust to normal-sense of shear movements beneath the wedge roof (Fig. 4a-ii, b-ii, 5a-ii, d-ii). For a given ϕ, decreasing μ_r causes the normal-sense shear field to shrink, and finally disappear when μ_r is extremely low ($\sim$10), and the whole wedge is dominated by thrust-type shear (Fig. 4c-ii). For $\mu_r \leq \sim 10^2$, the OP undergoes deformations in response to the shear stress generated at the wedge-slab interface (Fig. 4b-ii, c-ii, 5d-ii, f-ii). The addition of slab advance kinematics induces strong sub-horizontal shortening, combined with thrust shear in the OP. On the other hand, the slab rollback, as shown earlier for the wedge with rigid OP, the entire wedge is affected by thrust shear when ϕ is neither extremely low nor high (Fig. 5b-ii, e-ii). In contrast, higher ϕ conditions develop normal shear with sub-vertical ISA_{min} axes in the trench-ward side of the wedge (Fig. 5c-ii, f-ii). For moderate to low viscosity ratios ($\mu_r \leq \sim 10^2$), the slab rollback is associated with considerable sub-horizontal extension (ISA_{max}) in the overriding plate, away from the wedge (Fig. 5f-ii).

3.1.3 Influence of taper angle

Accretionary wedges can be narrow or wide, depending on the sediment influx and outflux of sediments into or from the wedge (Clift and Vannucchi, 2004; Cloos and Shreve, 1988) and the effects of other factors, such as subduction geometry (Pusok et

https://doi.org/10.5194/egusphere-2025-2909
Preprint. Discussion started: 12 August 2025

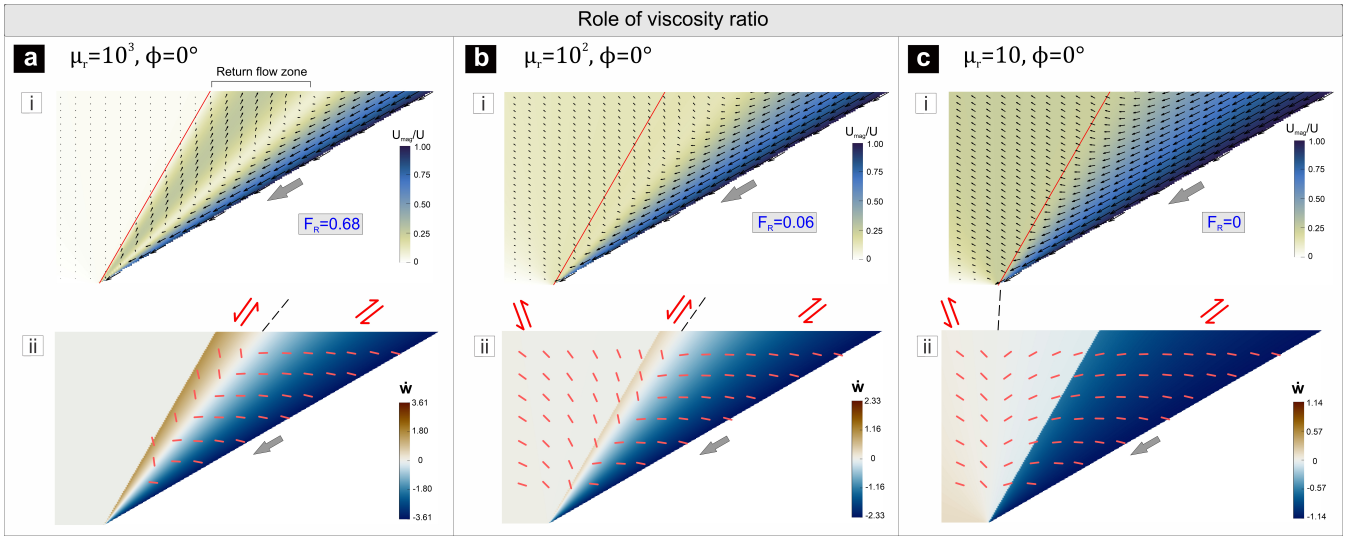

Figure 4. Velocity and vorticity fields in wedges with deformable wall settings undergoing slab-parallel subduction. θ_1 = 30°, and α = 30°. Decrease in wall to wedge viscosity ratio (μ_r) lowers F_R.

.

al., 2022). Our analytical solutions show that increasing θ_1 strengthens the return flux in a wedge (Fig. 6a-i, b-i, c-i). For ϕ = 0° and $\mu_r = 10^2$, an increase in θ_1 from 15° to 120° increases F_R from 0 to 0.97. Narrow wedges with $\theta_1 < \sim 15°$ do not produce any return flows (Fig. 6a-i) when μ_r is low to moderate ($\leq \sim 10^2$). In such conditions, the flows fails to redirect them back to the surface as they are strongly deflected towards the OP, which becomes more pronounced when the plate convergence involves slab advance. This kinematics implies that the wedge - OP interface will migrate forward, resulting in widening of the wedge (Moulas et al., 2021).

Large-taper wedges (θ_1 = 120°) develop thrust shearing in a bi-vergent configuration, as illustrated in Fig. 6c-ii. The oppositely verging thrust-shear zones are separated by a zone of normal-sense shearing. As discussed in the previous subsection 3.1.2, for a given μ_r, the wedge reverses the shear sense in a specific range of ϕ, which widens with increasing θ_1 (see section 3.3), implying that wider wedges are expected to develop shear reversal in the OP side (Fig. 6b-ii, c-ii). In contrast, narrow wedges with moderate to low μ_r ($< \sim 10^2$) never produce a condition of shear reversal, but allow the OP to accommodate considerable deformations (Fig. 6a-ii).

3.1.4 Role of the OP velocity

The overriding plates often experience a trench-ward velocity (U_{op}) due to far-field tectonic stresses or drag of the underlying mantle flows (Cerpa and Arcay, 2020; Jarrard, 1986; van Dinther et al., 2010). We use the present analytical solutions to investigate the effects of U_{op} on wedge flows. In case of no slab rollback, addition of U_{op} strengthens the convergence within the wedge, resulting in extrusion of the wedge materials from its roof regions to the surface (Fig. 6d) (Nettesheim et al., 2018).

https://doi.org/10.5194/egusphere-2025-2909
Preprint. Discussion started: 12 August 2025

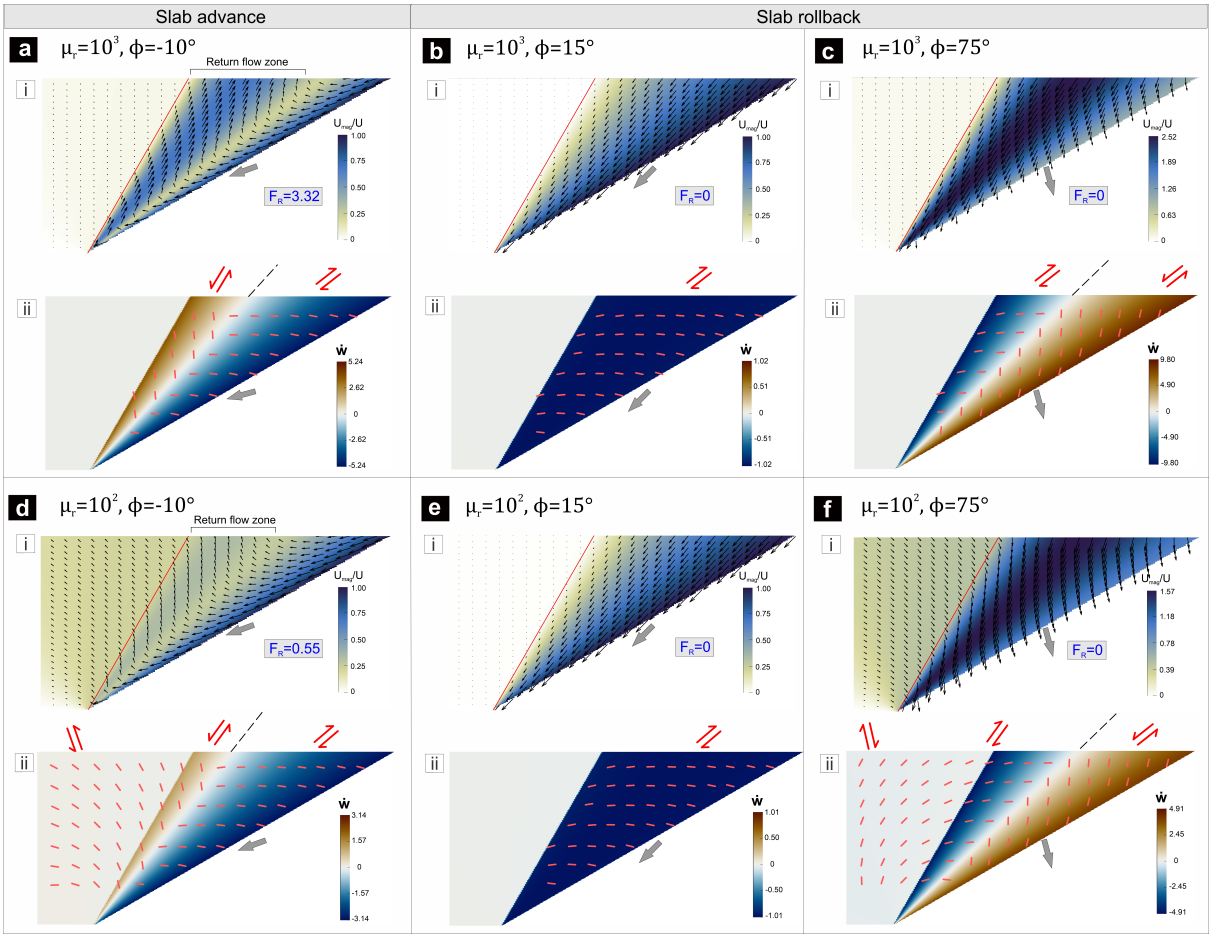

Figure 5. Effects of subduction obliquity (ϕ) and viscosity ratio (μ_r) on the velocity and vorticity fields in wedges. θ_1= 30°, and α = 30°.

.

For relatively lower rollback velocities (e.g., ϕ = 15°), the wedge shows curvilinear flow trajectory with upward convexity (Fig. 6e), as observed in some of the numerical models (e.g., Candioti et al. (2021)), implying that crustal materials under a steady state kinematic state of the wedge would be extruded and then recycled back to deeper regions. High rollback velocities, in contrast, facilitate the burial process of wedge materials with the subducting slab, allowing their little or no subsequent uplifts (Fig. 6f).

3.1.5 Effects of subduction dip

For a constant dip of the wedge-OP interface, decreasing slab dips give rise to increasing taper angles, which in turn facilitate the return flux (F_R) within the wedge. A steep dip of the wedge-OP interface yields higher extrusion rates (higher vertical component of velocity in Cartesian xy-frame) of the extruding wedge materials (see also Sanhueza et al. (2022)). However,

https://doi.org/10.5194/egusphere-2025-2909
Preprint. Discussion started: 12 August 2025

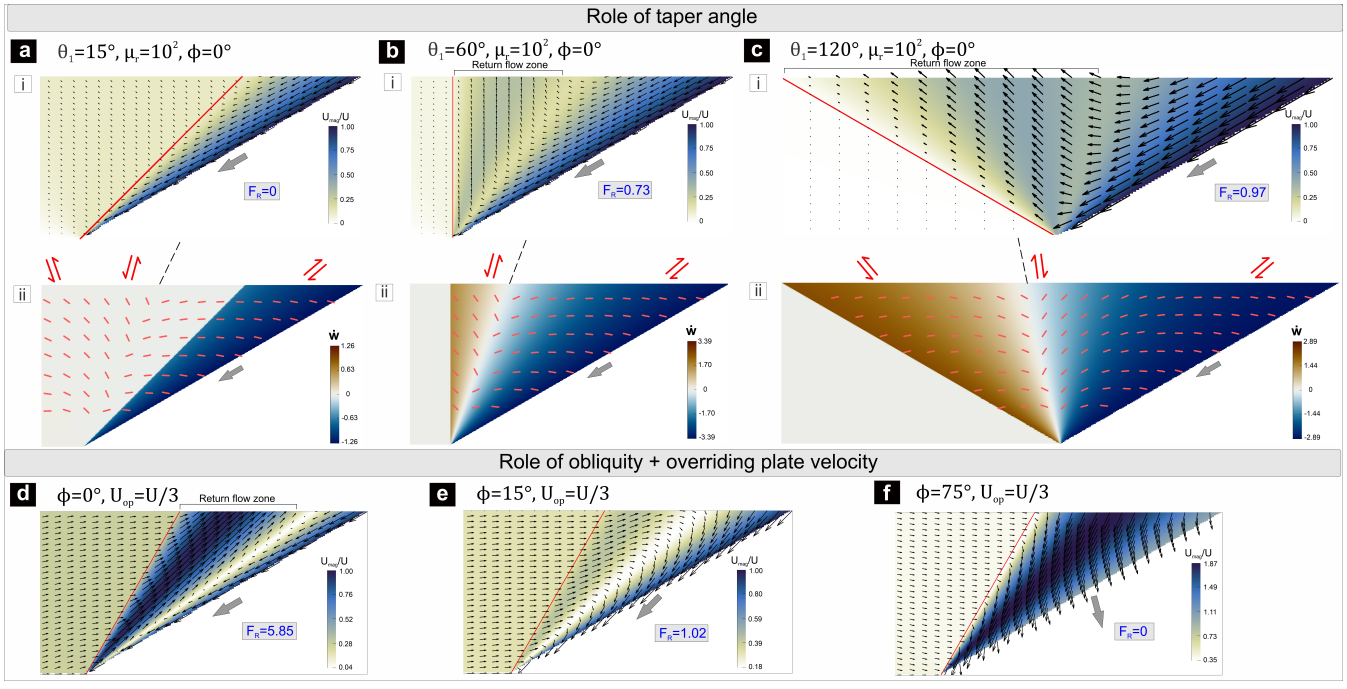

Figure 6. (a)-(c) Influence of taper angle (θ_1) on the kinematics of wedges in settings undergoing slab-parallel subduction. (d)-(f) Effect of trench-ward moving overriding plate movement (U_{op} = U/3) on the flow patterns of wedges: μ_r = 10^2, and α = 30°.

.

steeply dipping slabs generally exhibit high rollback velocities (hence increase in ϕ) due to slab pull force (Stegman et al., 2010), which in turn affect the wedge kinematics. From a dynamic point of view, lower subduction dips allow the convergent system to transmit higher stresses to the wedge and the overriding plate, and give rise to intense deformations in the forearc region (Chemenda et al., 2000; Guillaume et al., 2009).

3.2 Conditions for return flows

The analytical results discussed above suggest that the return flows in accretionary wedges, which play the most crucial role in deep-crustal exhumation processes can occur under specific conditions. The role of each factor in setting the return flows is summarized in Fig. 7. It can be readily seen that appreciable return flows ($F_R > 0.5$) occur in the following conditions: low ϕ (usually $< 5°$), high μ_r ($\geq \sim 10^3$) and high θ_1 ($\geq \sim 30°$). Wedges with large taper angles produce strong return flows, independent to the OP viscosity. Narrow wedges, i.e., low θ_1 (e.g., 15°) become almost devoid of any focused return flows, unless the OP is rigid or has high viscosity ($\mu_r > 10^3$). A strong overriding plate accommodates little strains, forcing the viscous flows to localize within the wedge. Increase in μ_r thus promotes the return flux. The return flow is also facilitated by the slab advance ($\phi < 0°$), but countered by the slab rollback process in subduction zones (Fig. 3, 5). These contrasting flow kinematics originate from the competing dynamics of two processes: dominance of a downward flow, induced by the

https://doi.org/10.5194/egusphere-2025-2909
Preprint. Discussion started: 12 August 2025

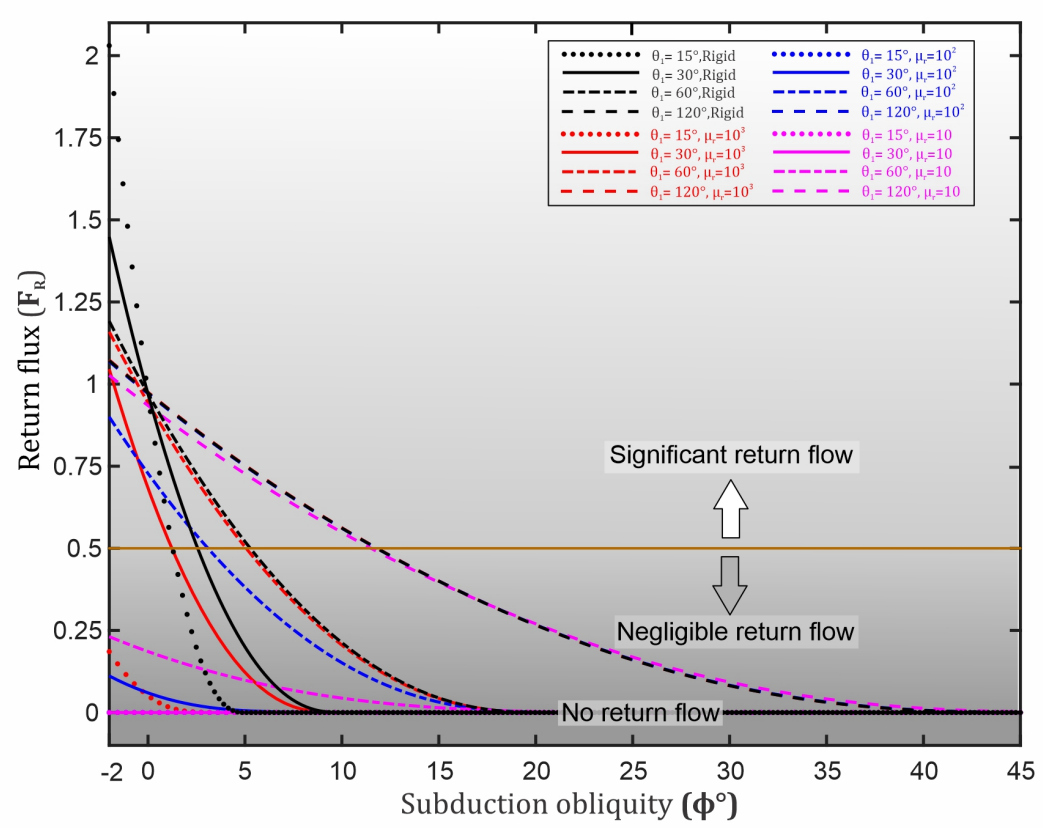

Figure 7. Calculated plots of return flux (F_R) as a function of the subduction obliquity (ϕ), viscosity ratio (μ_r), and taper angle (θ_1). Note that significant return flux ($F_R > 0.5$) occurs when μ_r is large ($\geq \sim 10^3$), and there is no slab rollback ($\phi \sim 0°$ or negative).

.

subducting slab drag, and an upward flow, driven by a negative upward dynamic pressure gradient along the wedge (Fig. 1c). The first process enables the burial mechanism of the wedge materials, whereas the second process forces the materials to extrude up, setting in return flows. The analytical results suggest that deformable OP settings with high μ_r, low ϕ, and large θ_1 develop strong pressure gradients along the wedge (Fig. S1 and S2 in supplement S1), which leads to the generation of return flows. However, progressive increase in ϕ lowers the pressure gradient and then reset its trend in the reverse direction (Fig. S2 in supplement S1, see also Fig. 10). This finding explains the absence of return flows in wedges where the slab rollback is active. Among other factors, trench-ward OP velocity can also facilitate the return flux in a wedge (Fig. 6d).

https://doi.org/10.5194/egusphere-2025-2909
Preprint. Discussion started: 12 August 2025

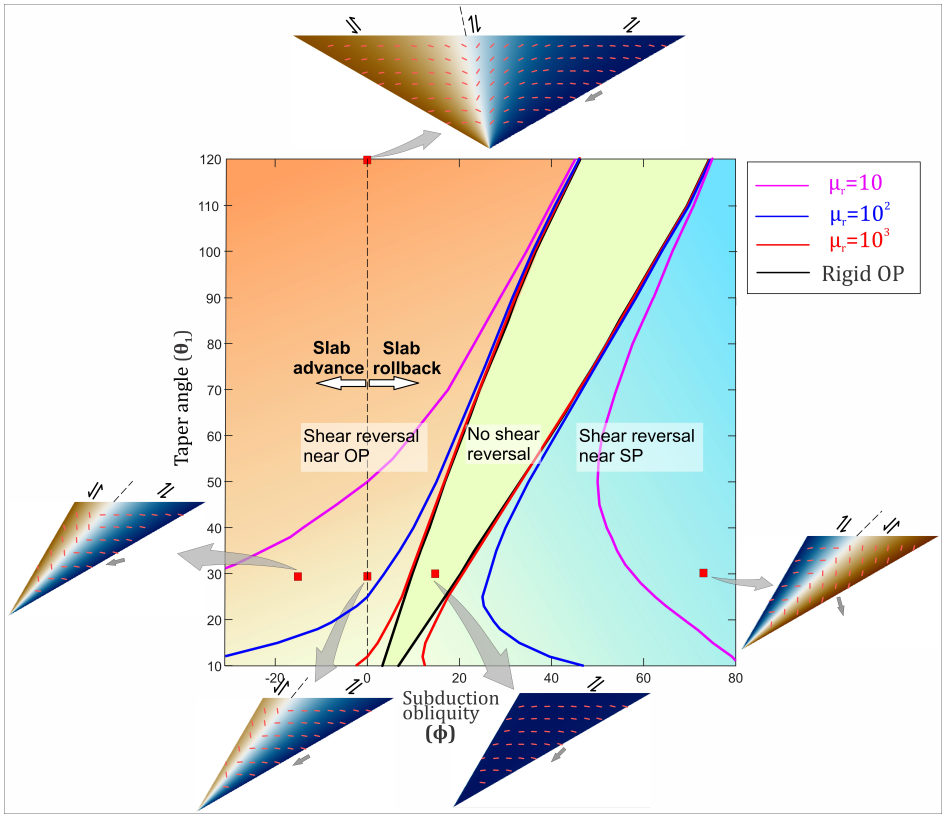

Figure 8. Fields of 'shear reversal' and 'no shear reversal' across the wedges in a parametric space defined by subduction obliquity (ϕ), taper angle (θ_1), and viscosity ratio (μ_r). To the left and right sides of the central 'no shear reversal' field, shear sense reverses differently, as shown by the vorticity regimes in the wedges ($\mu_r = 10^3$) at various positions of the field diagram.

.

3.3 Strain fields in wedges

For the model boundary conditions considered in this theoretical analysis, accretionary wedges accommodate deformation mostly by simple shear, although the sense of shearing can vary across the wedge, depending on the parametric conditions. The varying kinematic patterns are shown as a function of ϕ, θ_1, and μ_r in Fig. 8.

Three distinct modes of deformation can be recognized in the field diagram, each with a characteristic vorticity pattern. The central part of the diagram defines a field of no shear reversal, i.e., the whole wedge is characterized by the same shear sense, as imposed by the SP. For a low slab rollback velocity (i.e., low positive ϕ), the wedge shows no shear reversal unless the wedge taper angle is significantly large. The central field is bounded by two lines, the locus of which varies with μ_r. The field of no shear reversal widens with decreasing μ_r. To the left and right of this field, the shear sense reverses in the upper (i.e., near the OP) and lower (i.e., near the SP) regions of the wedge, respectively. The variation in the wedge kinematics is essentially a consequence of the interplay between the slab-driven Couette flow and the dynamic pressure-driven Poiseuille flow (Grujic

https://doi.org/10.5194/egusphere-2025-2909
Preprint. Discussion started: 12 August 2025

et al., 2002; Mancktelow, 1995). The relative dominance of these two flows determines the pattern of shear within the wedge. For high μ_r, slab-parallel subduction or those accompanied by slab advance or extremely slow slab rollback, develops large overpressures in the region close to the wedge tip (discussed later in section 4.3), which facilitates the Poiseuille flows. In such a situation, the slab-driven shear induces clockwise vorticity throughout the wedge, whereas the pressure-driven flow induces clockwise and anticlockwise vorticity in the lower and upper segments of the wedge, respectively. The lower part of the wedge thus undergoes thrust shear, whereas the pressure-driven flows creates normal shearing in the upper part of the wedge. On the other hand, for high μ_r, large rollback velocities (i.e., high ϕ) induce tectonic underpressure, resulting in a negative pressure gradient towards the tip that creates Poiseuille flows with downward velocity. Such conditions lead to localization of normal and thrust shearing in the lower and upper parts of the wedge, respectively. For low rollback velocities, the wedge develops gentle (positive or negative) dynamic pressure gradients, and the Couette flow dominates over the Poiseuille flow, as the negative P_d due to slab rollback is compensated by the positive P_d due to subduction (see section S1 in supplement S1). Such a dynamic condition favours the Couette flows, which give rise to dextral shearing throughout the wedge.

Wide wedges with large θ_1 show weak effects of slab migration (advance or rollback) on the generation of dynamic pressures in them. This condition favors the occurrence of positive P_d, and shear reversal across the wedge, even for relatively high ϕ values (Fig. 8). When μ_r is low, for subduction, with or without slab migration (advance or rollback), the direction of maximum P_d-gradient is not along the wedge, but towards the OP (see Fig. S1c in supplement S1). The Poiseuille flows induces significant deformations in the overriding plate, but not much effective in the wedge deformations. Low μ_r conditions thus facilitates thrust-sense shearing in the wedge. This explains the occurrence of a wider field of 'no shear reversal' for lower μ_r.

4 Observations in physical experiments

Physical experiments are often useful to validate analytical results and their interpretations. A series of laboratory experiments were performed to decipher the flow patterns in wedges with deformable walls and varying boundary kinematics, as described in the preceding sections.

4.1 Laboratory model setup

The wedge, made up of polydimethylsiloxane (PDMS), behaves as Newtonian viscous fluid (viscosity $\sim 10^4$ Pa s) at strain rates below 10^{-2} s^{-1} (Weijermars, 1986). The wedge had a height of ~4.5 cm, and its width narrowed down from ~5.3 cm at the top to ~0.8 cm at the base (Fig. 9a). For one set of experiments, the wall of the wedge was made up of high-viscosity modelling clay (viscosity $\sim 10^6$ Pa s), while in the other set, it was made up relatively low-viscosity mixture of modelling clay and PDMS (1: 10 ratio). The base of the wedge had a dip of 45°, and the contact between the wedge and its deformable wall was vertical. Such vertical contact reduces the effect of buoyancy forces on the kinematics of the wedge. In a reference frame fixed with respect to the buttress at the base of the deformable wall, the base of the wedge was moved parallel or oblique to itself to simulate shear, oblique shortening or oblique extensional kinematics (Fig. 9b, c). The detailed description of the model velocity boundary conditions is provided in the supplement S1 (section S2). Photos of the model vertical section were

https://doi.org/10.5194/egusphere-2025-2909
Preprint. Discussion started: 12 August 2025

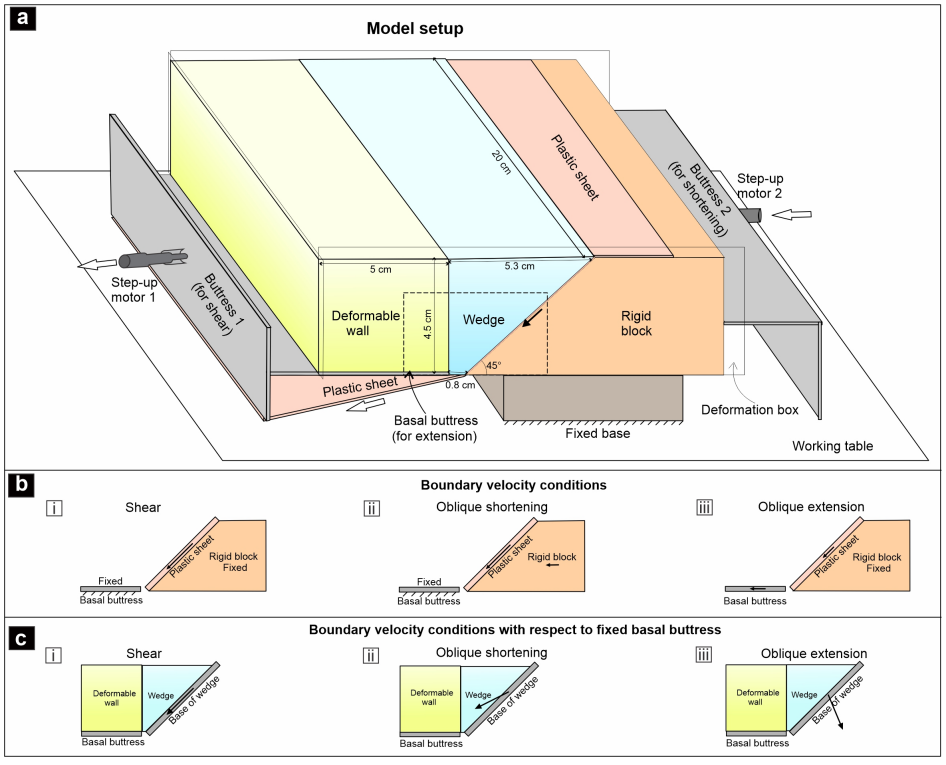

Figure 9. (a) Laboratory model setup used for wedge experiments (details provided in the text). Dashed rectangle shows the region of interest. (b) Velocity conditions imposed at the model boundaries to simulate shearing, oblique shortening, oblique extension in the model. (c) Boundary velocity conditions with respect to a fixed basal buttress.

taken regularly, and they were processed through to obtain the incremental displacement field using the PIVLab (Thielicke and Stamhuis, 2014), an open-source image correlation software run in MATLAB.

The model had a length of 20 cm in y-direction, and its upper surface was set free. This allows a deformation regime close to plane strain condition with negligible deformation along the y-direction, especially in the earlier stages of the experiments. Furthermore, the experiments were done at a relatively higher strain rates of $\sim 10^{-3}$ s^{-1}, so that the shear stresses imposed at the boundaries primarily drive the deformation and gravitational stresses play negligible role in it. The deformation box walls were lubricated with soap to reduce the friction between the viscous materials and glass walls.

4.2 Key experimental findings

When the base of the wedge moves tangentially (i.e., $\phi = 0°$), the wedge develops effective return flow for the more competent wall ($\mu_r \approx 10^2$) (Fig. 10a-i). Although, part of the return flow is deflected towards the wall, the maximum vertical velocity (v_{max}) across the central part of the wedge is about 30% of the imposed boundary velocity (U). However, for a lower viscosity

https://doi.org/10.5194/egusphere-2025-2909
Preprint. Discussion started: 12 August 2025

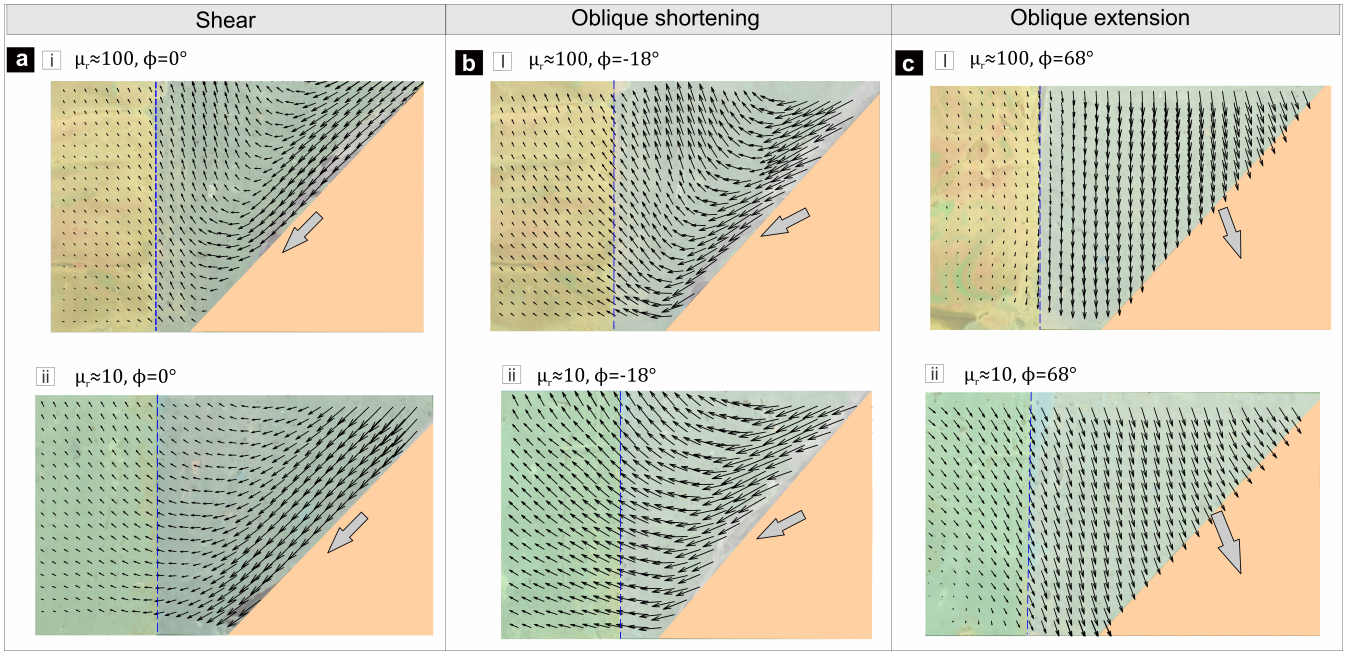

Figure 10. Flow patterns in experimental models with subduction obliquities (ϕ): 0°, -18°, and 68°, and viscosity ratios (μ_r): ≈ 10^2 and ≈10. Note that lower μ_r (≈ 10) gives rise to return flows significantly deflected towards the wall in shear and oblique shortening conditions.

.

ratio ($\mu_r \approx 10$), the return flow within the wedge is strongly deflected towards the wall (Fig. 10a-ii) and the v_{max} within the wedge is only about one-sixth of U. In case of oblique shortening (ϕ = -18°), for both viscosity ratios, the v_{max} within the wedge attains high values, comparable to U. The deflected return flow causes deformation within the wall (Fig. 10 b-i, ii). For lower μ_r, the wall of the wedge is also uplifted at high rates (∼0.6 U). For oblique extension (ϕ = 68°), the opening of the narrowing end of the wedge causes the wedge materials to flow downward (Fig. 10 c-i, ii). This downward velocity locally exceeds the given U value. In case of low μ_r, the downward flow within the wedge, also drags the deformable wall towards itself.

The findings of our theoretical analysis are grossly consistent with the experimental observations. However, in contrary to the theoretical prediction, the vertical velocity (v) in experimental models increases close to the upper free surface of the wedge (Fig. 10 a, b). This discrepancy occurs because the 'free surface' in the analytical solutions are considered to be infinite distance away from the corner point (section 2.2.2), whereas our experimental setup is finite. Also, the friction between the wedge and the model wall, might locally reduce the velocity. Nevertheless, both experimental observations and analytical model results, suggest that return flow within the wedge is favorable only for high viscosity contrast between the wedge and its deformable wall, and when there is no bulk extension across the wedge.

https://doi.org/10.5194/egusphere-2025-2909
Preprint. Discussion started: 12 August 2025

5 Discussion

5.1 Exhumation of high P metasediments by return flows: model vs nature

Subduction zones generally host distinct types of high-pressure low-temperature (HP–LT) metamorphic rocks: metamorphosed oceanic sediments, oceanic crust (+ mantle), and continental crusts, each of them records its own exhumation characteristics (Agard et al., 2009, 2001; Burov et al., 2001; Gerya et al., 2002; Angiboust et al., 2012). The exhumation of oceanic sediments in accretionary wedges usually occurs as a syn-convergent steady process operating on tens of million years, whereas oceanic crustal fragments record episodic exhumation events corresponding to different stages of subduction (Husson et al., 2009; Yamato et al., 2007; Wang et al., 2019). They also show varying modes of occurrences in the subduction settings. High pressure metasediments occur as extensive, continuous metasedimentary outcrops with smooth, progressively increasing P-T conditions (Agard et al., 2001; Ernst, 1993). On the other hand, exhumed oceanic crustal bodies form distinct slices of units, often associated with serpentinites, and exhibit contrasting P-T peaks, as reported from the Western Alps (Agard et al., 2009; Schwartz et al., 2001; Angiboust et al., 2012). Previous studies have used the corner flow mechanism to explain the exhumation of high-pressure metasedimentary rocks in terms of return flows in accretionary wedges (Allemand and Lardeaux, 1997; Gerya et al., 2002; Shreve and Cloos, 1986). The present theoretical analyses suggest that accretionary wedges can produce such return flows only in specific conditions determined by a number of parameters, such as subduction obliquity, viscosity of the overriding plate, and taper angle of the wedge, as shown in Fig. 7.

The relative volume of exhumed high-pressure metasedimentary rocks varies significantly in the accretionary wedges of convergent settings. Agard et al. (2009) have provided estimates recycled volume budgets of subducted sediments, ∼80–90% in the Cascades, whereas 30–50% in the Western Alps. However, the estimates yield remarkably low values, <1% in the Chile and Franciscan complex. Although low preservation potential of blueschist facies rocks or differential erosional effects are possible factors for such variations, the flow kinematics in the accretionary wedge seems to be one of the most influential factor in determining the amounts of uplifted masses. Our theoretical estimates suggest that return flows become a rigorous process under limited kinematic, rheological and geometrical conditions. For example, the ratio of returned to subducted material volumes at any instant within a steady state accretionary wedge (F_R) is high (> 0.5), as observed in the Cascades and the Western Alps (Agard et al., 2009). The present theory predicts this estimate for the following specific conditions: 1) subduction with little or no slab rollback, 2) high relative strength of the overriding plate ($\mu_r \geq \sim 10^3$), and 3) large wedge taper angles (θ_1). For small taper angles ($\theta_1 \leq \sim 30^\circ$) and weak overriding plates ($\mu_r \leq \sim 10^2$), the settings hardly return materials within the wedge, the quantity of which can be further reduced by slab rollback (Fig. 4b-i, 5b-i). This theoretical finding perhaps explains the scarcity or absence of exhumed high P metasediments in accretionary wedges like Chile. For relatively weak overriding plates (OP), the return flows originating from deeper regions eventually deflect towards the overriding plate, resulting in exhumation of both the wedge and OP materials in the retroside regions (Butler et al., 2011), at extremely slow rates ($< 0.1\ U$ for $\mu_r = 10^2$) (Fig. 11a). However, such sluggish uplift processes do not support them to travel much in the upward direction. Extremely weak ($\mu_r \leq \sim 10$) OP settings, however, produce flows closely similar to those formed in a single (i.e., $\mu_r = 1$) corner model with a large taper angle, enabling the crustal materials to uplift at considerable velocities and accumulate

https://doi.org/10.5194/egusphere-2025-2909
Preprint. Discussion started: 12 August 2025

in the retroside of the wedge (Fig. 4c-i). Slab rollback at high velocities (keeping the OP fixed) suppresses the return flows, instead it facilitates leaking of crustal materials through a narrow passage into the mantle (Fig. 3c-i, d-i, 4b-i, c-i, e-i, f-i), a phenomenon commonly known as *subduction erosion* (Clift and Vannucchi, 2004; von Huene and Scholl, 1991). However, the same tectonic setting favours exhumation in other rocks, such as oceanic crustal units, low-density continental blocks and mantle rocks (Brun and Faccenna, 2008; Husson et al., 2009; Wang et al., 2019), as the slab rollback and associated upper plate extension create free spaces within the lower- or upper plate-side of the fore-arc, setting a dynamic condition for the exhumation of (U) HP rocks from mantle depths. On the other hand, our model results suggest that a period of slab advance during subduction can facilitate the extrusion process in the wedge, resulting in exhumation of deep-crustal materials (Fig. 3b-i, 5a-i, d-i, 10b-i, ii).

The calculated extrusion velocities of HP-LT rocks in accretionary belts vary on a wide range, from <1 mm/yr to >1 cm/yr (see table 1b of Agard et al. (2009) and references therein), but they mostly lie in the order of mm/yr. In contrast, previous CF model studies yield extrusion velocities much higher than 1 cm/yr (Allemand and Lardeaux, 1997; Cloos, 1982; Gerya et al., 2002), which perhaps occur due to the geometrical and kinematic boundary conditions chosen in the models. The present theoretical analysis, however, suggests that the return flows can be significantly slow due to specific mechanical and geometric conditions: low relative viscosities of the overriding plates ($\mu_r < \sim 10^3$) and small taper angles ($\theta_1 \leq \sim 30^\circ$) (Fig. 11a,b). For θ_1 = 30°, accretionary models with μ_r = 10^3 and 10^2 yield maximum vertical uplift velocities (v_{max}) about one-fourth to one-eighth of the subducting plate velocity (U), respectively (Fig. 11a), i.e., ∼7.4 mm/yr and 3.9 mm/yr for U = 3 cm/yr. As the material particles track curvilinear paths, they would be extruded mostly at velocities less than v_{max}, and their time-averaged velocity would be less than v_{max}. Our theoretical estimates are consistent with those (1-5 mm/yr) calculated from the Schistes Lustres complex in the Western Alps (Agard et al., 2001) and other accretionary belts (Brandon et al., 1998; Glodny et al., 2005; Ring et al., 1999). The theoretical results further indicate that syn-subduction slab rollback ($\phi > 0^\circ$), even small in magnitudes can again weaken the return flow kinematics, reducing the extrusion velocities to a large extent (< 1 mm/yr; Fig. 11a-d). Additionally, discrete slip along the wedge-subducting plate interface can also decrease the exhumation velocity (v), as v is directly proportional to the velocity (U) at the base of the wedge. Other mechanisms, such as gravitational spreading at shallow crustal level (Van Dinther et al., 2012), deformation localization, syn-subduction sediment accumulation can also contribute to a reduction in the exhumation velocity. Therefore, in contrast to the prevailing notion that the extremely slow exhumation rates result solely from erosion (Brandon et al., 1998; Platt, 1993) and other reasons discussed above, our model findings suggest that corner flow processes can also modulate the kinematics of extrusion of deep HP rocks to the surface at slow rates.

High-pressure rocks in many convergent belts record unusually high uplift rates. As an example, the Ampelos/Dilek nappe of the Cycladic blueschist unit in the eastern Aegean underwent extrusion at rates 3-3.5 cm/yr during incipient collision of the Anatolian microcontinent with Eurasia (Ring et al., 2007). Our theoretical analysis suggests that mechanically strong overriding plates ($\mu_2 > \sim 10^{22}$ Pa s) and/or significant slab advance ($\phi < 0^\circ$) kinematics form potential convergent settings for high-rate extrusion in wedges with moderate tapering angles (Fig. 9 a). Extremely fast uplift velocities ($> U$) of wedge materials are obtained in the models with continental collision (i.e., $\phi \approx$ -α) type settings. In addition, large crustal scale normal-sense shear

https://doi.org/10.5194/egusphere-2025-2909
Preprint. Discussion started: 12 August 2025

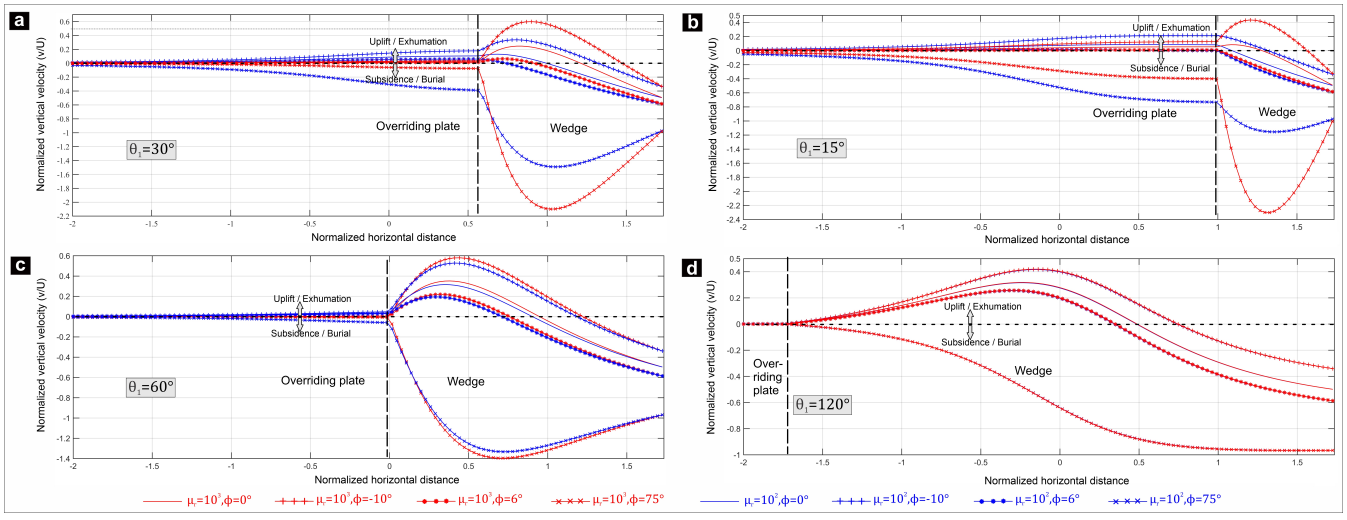

Figure 11. Vertical-velocity profile (at y = 10 km) across the wedge and the overriding plate for different θ_1 (a-d), μ_r, and ϕ. Positive and negative values of the vertical velocity indicate uplift/ exhumation and subsidence/ burial of wedge materials, respectively.

.

zones (or faults) within the wedge or at the wedge-overriding plate contact can exhume high P rocks at fast rates (Bento dos Santos et al., 2021; Searle, 2015). Presence of buoyant crustal blocks and erosion can further facilitate the extrusion kinematics (England and Holland, 1979; Ernst et al., 1997; Godin et al., 2006). The present theoretical estimates also account for relatively higher extrusion rates (∼1 cm/yr) in wider wedges with large taper angles (Fig. 11 c, d).

5.2 Deformation patterns

Accretionary wedge deformations have generally been explained using the critical taper theory in the framework of Coulomb rheology (Dahlen, 1990; Dahlen et al., 1984; Buiter, 2012). However, this rheological consideration may not provide good approximations for wedges thicker than ∼15 km as thermally activated ductile deformation mechanisms become significant in controlling the rheology of the wedge materials at depths (Pavlis and Bruhn, 1983; Platt, 1986). Viscous flow regimes below the brittle-ductile transition depth characterize the deformation patterns across the wedge (Fig. 1b, 2a). Our theoretical results reveal that wedge settings under specific conditions (presence of strong overriding plate, subduction or slab advance) produce two synchronous domains of shear deformations with opposite shear senses: thrust shear in the lower part and normal shear in the upper part of the wedge (Fig. 4a-ii, b-ii, 5a-ii, d-ii,8). The shear reversal is accompanied by a systematic variation of the strain fields, with sub-horizontal principal shortening axes close to the subducting plate, which reorient to become sub-vertical towards the overriding plate.

The shear reversal phenomenon has been reported from extruded rocks in several subduction (e.g., Hellenides (Ducharme et al., 2022), Western Alps (Agard et al., 2001), Sambagawa Belt (Osozawa and Wakabayashi, 2015)) and collisional (e.g., the Cycladic blueschist unit in the Eastern Aegean (Ring et al., 2007), Higher Himalayan Crystallines (Beaumont et al., 2001;

https://doi.org/10.5194/egusphere-2025-2909
Preprint. Discussion started: 12 August 2025

Grujic et al., 2002), the Porto–Viseu Metamorphic Belt in the Central-Iberian Zone (Bento dos Santos et al., 2021)) tectonic wedges. Considering a steady state flow kinematics, crustal materials following their burial to greater depths are recycled back to the surface by return flows and experience shear deformations in both lower and upper domains of the wedge. Consequently, they can record thrust-sense shear structures in them, overprinted by normal-sense shear structures during exhumation, as observed in the Cycladic Blueschist Unit at Fabrika (Ring et al., 2020). Such corner-flow driven complex tectonics can produce deformational structures under sub-horizontal shortening in the burial phase, which are superposed by structures related to sub-vertical shortening. Multiple structural fabrics develop in the course of a progressive tectonic event, without any change in the external kinematic frame (Richter et al., 2007). The strain fields at the time of exhumation indicate sub-vertical crustal shortening and tectonic thinning (Feehan and Brandon, 1999; Ring and Brandon, 2008), manifested in sub-horizontal foliations, which are superposed on earlier tectonic structures, such as folds and fabrics in several paleo-accretionary wedges e.g., San Juan-Cascade nappes, coastal accretionary belt of Chile (Richter et al., 2007; Muñoz-Montecinos et al., 2020).

Many tectonic wedges show deformation localization preferentially along two bounding synchronous shear zones with opposite shear senses: one with normal and the other with reverse sense of shear, leaving the rest part in the wedge unaffected (Grujic, 2006). Crustal scale extensional (normal) shear zones that localize in the upper part of the wedge largely control the exhumation of high grade metamorphic rocks beneath low grade rocks in subduction and collisional settings (Searle, 2015). The extensional shearing in the deeper region gives way to normal faulting at the shallow crustal level in the hinterland as the return flows result in vertical crustal uplift in the rear of the wedge (Fig. 11). This uplift develops normal faulting to retain the stability (Platt, 1986). The normal faults further assist in the exhumation of high P materials, especially at shallow crustal depths (Platt, 1993; Ring et al., 1999).

The model results presented in the preceding section indicate that the deformation styles in convergent settings strongly depend on a number of geometric and kinematic parameters: slab motion, overriding plate's relative viscosity (μ_r), and wedge taper angle (Fig. 8). For moderate to high μ_r ($\geq \sim 10^2$), subduction, with or without slab advance (i.e., zero or negative ϕ), can produce shear reversal, as discussed above, in the wedge. The shear reversibility disappear if μ_r is low ($\sim< 10^2$) and the slab retreat (i.e., positive ϕ) becomes active. For a moderately tapering wedge, the later can give rise to thrust-sense shearing in the entire wedge (Fig. 3c-ii, 4c-ii, 5b-ii, e-ii), with the exceptions that high slab rollback velocities develop normal-sense (with subhoizontal extension) and thrust-sense shearing close to the subducting and the overriding plate, respectively (Fig. 3d-ii, 5c-ii, f-ii). For a vertical wedge-OP interface, , the wedges localize normal-sense shear in their rear parts, leaving the rest parts under thrust-sense shear (Fig. 6b-ii), as widely reported from analogue experiments (Chattopadhyay and Mandal, 2002; Luján et al., 2010). In contrast, wider wedges characterized by oppositely-dipping walls transforms the shear patterns into doubly-vergent thrust sense shears, separated by a zone of normal-sense shear in their axial regions (Fig. 6c-ii). This theoretical pattern agrees well with those produced in analogue experiments on viscous wedges (Deville, 2023; Luján et al., 2010).

In subduction zones the subducting oceanic slabs can induce strong deformations in their overriding plates, often manifested in characteristic topographic developments (Buiter et al., 2001; Dasgupta and Mandal, 2018; Hampel and Pfiffner, 2006; Shijie Zhong and Gurnis, 1994). Previous studies suggest that the forces responsible for such OP deformations originate in several ways, viscous drag at the base of the overriding plate, suction effects between the subducting and the overriding plate, and

https://doi.org/10.5194/egusphere-2025-2909
Preprint. Discussion started: 12 August 2025

shear generated at the slab interface (Chen et al. (2017); Schellart (2024), and references therein) A detailed discussion of their independent role is beyond the scope of this study. However, our theoretical analysis suggests that the shear force generated by the subducting plate can induce large crustal deformations in the overriding plate only under specific conditions constrained by the overriding plate viscosity, and the subduction kinematics (slab advance vs. rollback). High μ_r ($> \sim 10^3$) allows the overriding plates to accommodate little shear exerted by the wedge flows. Consequently, they undergo little deformations ($\dot{\varepsilon}_{xy}$ $<10^{-16}$ s^{-1}) and hardly produce topographic uplifts. This condition rather facilitates the return flows in localizing high uplifts within the wedge rear. Moderate to low μ_r favours the overriding plate to transmit the wedge-induced shear and undergo deformations with considerable uplift rates (Fig. 11a, b). This condition thus results in a widely uplifted region in the forearc. Such fore-arc uplifts are more pronounced in wedges with large taper angles (which is equivalent to μ_r = 1) (Fig. 11c, d). This interpretation explains the occurrence of broad forearc highs in many long-lived, large accretionary complexes, such as the Lesser Antilles, the Alaskan, the Makran, and the Cyprus-Anatolian margin (Pavlis and Bruhn, 1983). Several authors have presented similar interpretations for the tectonics of fore-arc highs, emphasizing the role of upward viscous flows in the lower crust (Fernández-Blanco et al., 2020; Pavlis and Bruhn, 1983). Our theoretical analysis shows that, for a hinterland-dipping wedge-OP boundary, part of the overriding plate, close to the wedge, develops normal-sense shear. Away from the wedge, the strain field is replaced by retro-shear with sub-horizontal shortening. The uplift velocity of the fore-arc region increases when the slab advance accompanies subduction (Fig. 10b, 11). The slab rollback, in contrast, forces the overriding plate to flow towards the wedge, resulting in fore-arc subsidence, as also observed in the physical experiments (Fig. 10c-i, ii). These results are in agreement with the previous experimental results where the subduction setup produced fore-arc subsidence and sub-horizontal extension during the trench retreat (Chen et al., 2017; Xue et al., 2022).

5.3 Can accretionary wedges generate significant tectonic overpressures?

Pressure estimates from geobarometry of exhumed metamorphic rocks are generally equated with the depth (h) of metamorphism and reconstruction of the tectonic history, assuming that the lithostatic pressure, $p = \rho g h$, where ρ is the average rock density, and g is the gravitational acceleration. However, this condition applies essentially to a static fluid condition. A direction of studies accounts for the effects of dynamic pressure (produced by fluid flows), calculated as the difference between the total pressure (or mean stress) and lithostatic pressure, i.e., excess pressure (Mancktelow, 1995; Petrini and Podladchikov, 2000). This can be hundreds of MPa or even several GPa higher (tectonic overpressure) or lower (tectonic underpressure) than the corresponding lithostatic pressure. Several numerical model studies claim the possibility of tectonic overpressure (TOP) in subduction-collisional zones (Li et al., 2010; Marques et al., 2018; Raimbourg and Kimura, 2008; Reuber et al., 2016). Mancktelow (1995); Moulas et al. (2021) analytically determined tectonic overpressure in downward tapering subduction channels bounded by rigid and deformable wall(s), respectively. We use our analytical solution to evaluate the maximum dynamic pressure (P_{dmax}) in a wedge, which is found to be a function of several parameters: subduction velocity vector (U: both magnitude and direction), overriding plate velocity (U_{op}), the taper angle (θ_1) and viscosity (μ_1) of the wedge, and overriding plate-wedge viscosity ratio (μ_r). The following conditions: high μ_1, μ_r, U, U_{op} and low ϕ (negative), θ_1 values give rise to higher values of P_{dmax} (Fig. 12).

https://doi.org/10.5194/egusphere-2025-2909
Preprint. Discussion started: 12 August 2025

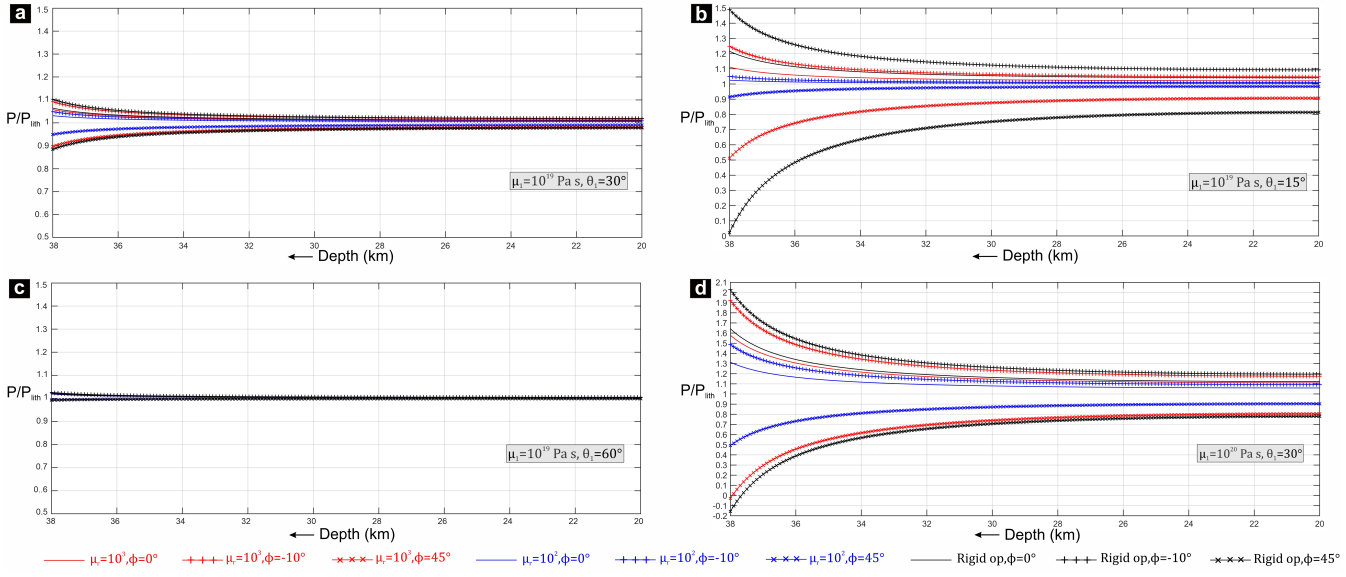

Figure 12. Plot of the total pressure (P), normalized to the lithostatic pressure (P_{lith}) along the acute bisectors of the wedges for varying μ_1, θ_1, μ_r, and ϕ. P_{lith} is calculated assuming the overburden density as 2800 kg/m^3.

.

The magnitude of dynamic pressure in the downward-tapering wedge increases towards the tip and theoretically becomes infinity at the wedge tip (S-point), a singularity point. Natural accretionary wedges, however, are likely to possess a finite width at its base instead of terminating at a single point, as some volumes of the incoming sediments leak through the bottom of the accretionary wedges and form the deeper subduction channel (Agard et al., 2009). Hence, we find it reasonable to not consider the anomalously high dynamic pressure at the bottom 2 km of our model wedge. This gradient in dynamic pressure drives the exhumation of deep-crustal HP rocks (Fig. 1b). The dynamic pressure scales linearly with the viscosity (μ_1) of the wedge materials. The choice of viscosity values is a critically important issue in the dynamic pressure calculations. Field data, compiled from a range of exhumed subduction complexes and experimental rock deformations suggest μ_1 in the ranges of $\sim 10^{18}$ to 10^{20} Pa s at the subduction interfaces (Abila et al., 2025). For our calculations, we thus consider $\mu_1 = 10^{19}$ Pa s for metasedimentary rocks in the wedge (Behr and Becker, 2018). Our analytical results show that for a moderate subduction velocity of 3 cm/yr and a moderate taper angle of 30°, maximum TOP is less than 8% of the lithostatic pressure in a wedge with $\mu_1 = 10^{19}$ Pa s (Fig. S1 in supplement S1). The magnitude of P_{dmax} reduces further to $< 4\%$ with a decrease in the overriding plate viscosity, $\mu_2 \leq 10^{21}$ Pa s (Fig. 12a, b, c). The magnitude of dynamic pressure can be of one order higher in wedges with higher viscosity ($\mu_1 \geq 10^{20}$ Pa s) (Fig. 12d). Hence, some high-pressure rocks record extremely fast exhumation rates, as calculated from lithostatic pressure approximations, which might reflect the influence of TOP at relatively shallow depths ($<$ $\sim$40 km) (Marques et al., 2018). Presence of high viscosity units can also lead to higher TOP in less competent materials with lower deviatoric stress, due to force-balance requirements (Schmalholz et al., 2014; Schmalholz and Podladchikov, 2013). TOP

https://doi.org/10.5194/egusphere-2025-2909
Preprint. Discussion started: 12 August 2025

also increases for narrower wedges with lower taper angles (Fig. 12b). Extremely small taper angles, however, does not produce significant dynamic pressure, unless the overriding plate is relatively very strong (viscosity $> \sim 10^{22}$ Pa s). A weak overriding plate cannot sustain a narrow wedge and for a steady state condition, the wedge will become wider with time (see the velocity vectors of the wedge-overriding plate interface in Fig. 4b-i, c-i, 5d-i, 6a-i), as also discussed by Moulas et al. (2021). Tectonic overpressure becomes extremely low ($< 2\%$) in wider wedges (Fig. 12c). In addition, our theoretical results indicate that the process of slab advance can elevate the TOP in the subduction zone (Fig. S2 in supplement S1). On the contrary, slab rollback creates a condition of tectonic underpressure (TUP) within the wedge, the magnitude of which increases towards depth (Fig. 12). This negative pressure gradient towards depth causes significant burial of wedge metasediments. Underpressure within the wedge also drives flow in weak hanging wall towards the wedge, causing overriding plate extension and narrowing of the wedge (Fig. 5f-i, ii). TUP increases with increase in slab rollback velocity (higher ϕ); however, for a steady state condition, these wedge materials are not exhumed from a great depth.

To summarize, several previous studies have emphasized the importance of tectonic overpressure in exhumed HP units. The present study suggests that for accretionary wedges comprising of low viscosity sediments, the nonlithostatic pressure component is small, generally in the order of tens of MPa (Reuber et al., 2016; Yamato et al., 2007). Significant tectonic overpressure can develop if any of these following conditions are satisfied: 1) wedges consist of materials of high viscosity, 2) the wedge is narrow with a strong hanging wall, and 3) the subduction involves slab advance.

6 Conclusions

A generalized analytical solution of the corner flow theory has been derived to study the kinematics of crustal flows in viscous accretionary wedges, with a special emphasis on the criticality of the conditions required for return flows and thereby exhumation of deep-crustal rocks in convergent tectonic boundaries. The analytical solution, supported by physical laboratory model experiments, suggest that the subduction obliquity (ϕ), overriding plate-wedge viscosity ratio (μ_r) and the taper angle (θ_1) of the wedge are principal factors in determining the velocity and strain fields within the accretionary wedge. The principal findings of this study are concluded in the following. 1) Accretionary wedges can produce focused return flows specifically in settings with $\mu_r \geq \sim 10^3$, $\theta_1 \geq \sim 30°$, and subduction with little or no slab rollback ($\phi \sim 0°$). The slab rollback ($\phi < 0°$) process drastically weakens the return fluxes in the wedges. 2) Return flow velocities in the deeper regions of wedges can range from $<$ 1 mm/yr to a few cm/yr. Slab advance ($\phi > 0°$) during the subduction promotes the vertical flow velocities, attaining maximum values comparable to the subduction velocity, provided the overriding plate is strong ($\sim\mu_r \geq \sim 10^{22}$ Pa s) and wedge taper angle is not low ($\theta_1 \geq \sim 30°$). 3) The shear sense may reverse across the wedge under a critical combination of the aforesaid parameters. 4) Weak overriding plates ($\mu_r < \sim 10^2$) accommodate significant amounts of global deformations, resulting in vertical uplifts over a broad region in the fore-arc regions. 5) Accretionary wedges comprising low-viscosity ($\sim 10^{19}$ Pa s) sediments are unlikely to develop large tectonic overpressures (or underpressures).

https://doi.org/10.5194/egusphere-2025-2909
Preprint. Discussion started: 12 August 2025

Code and data availability. The relevant data used to support the findings of this study are available in the article and in the supplement. MATLAB scripts are provided in the repository (10.6084/m9.figshare.29331581). These sample files can be used for the calculation and visualization of the analytical results and graphs presented in this work.

Appendix A

We show the detailed expressions of the eight equations used for deriving the eight constants A_i, B_i, C_i, D_i (i = 1, 2). These eight equations are derived from the eight boundary conditions. The velocity conditions at the wedge base (Eqn. 13) follow:

$$A_1 + D_1 = -Ucos(\phi) \tag{A1a}$$

$$-B_1 = -Usin(\phi) \tag{A1b}$$

At the Moho in the overriding plate (OP), the velocity boundary conditions (Eqn. 14) are expressed as:

$$A_2cos(\theta_2) - B_2sin(\theta_2) + C_2(sin(\theta_2) + \theta_2cos(\theta_2)) + D_2(cos(\theta_2) - \theta_2sin(\theta_2)) = -U_{op} \tag{A2a}$$

$$-(A_2sin(\theta_2) + B_2cos(\theta_2) + C_2\theta_2sin(\theta_2) + D_2\theta_2cos(\theta_2)) = 0 \tag{A2b}$$

Using the continuity condition for the two velocity components across the wedge-OP interface (Eqn. 15), we obtain the following relations:

$$\begin{aligned} A_1cos(\theta_1) - B_1sin(\theta_1) + C_1(sin(\theta_1) + \theta_1cos(\theta_1)) + D_1(cos(\theta_1) - \theta_1sin(\theta_1)) = A_2cos(\theta_1) - B_2sin(\theta_1) \\ +C_2(sin(\theta_1) + \theta_1cos(\theta_1)) + D_2(cos(\theta_1) - \theta_1sin(\theta_1)) \end{aligned} \tag{A3}$$

$$-(A_1sin(\theta_1)+B_1cos(\theta_1)+C_1\theta_1sin(\theta_1)+D_1\theta_1cos(\theta_1)) = -(A_2sin(\theta_1)+B_2cos(\theta_1)+C_2\theta_1sin(\theta_1)+D_2\theta_1cos(\theta_1)) \tag{A4}$$

Lastly, the continuity of normal and shear stress components across the wedge-OP interface (Eqn. 19) leads to:

$$(2\mu_1(D_1cos(\theta_1) + C_1sin(\theta_1)))/r = (2\mu_2(D_2cos(\theta_1) + C_2sin(\theta_1)))/r \tag{A5a}$$

$$-(2\mu_1(C_1cos(\theta_1) - D_1sin(\theta_1)))/r = (2\mu_2(C_2cos(\theta_1) - D_2sin(\theta_1)))/r \tag{A5b}$$

https://doi.org/10.5194/egusphere-2025-2909
Preprint. Discussion started: 12 August 2025

By solving the eight equations above, we find the expressions of the eight constants:

$$
\begin{aligned}
A_1 = &-(2U\mu_1^2\theta_1^2 cos(\phi) - U_{op}\mu_2^2 cos(\theta_2) - U\mu_1^2 cos(\phi) + 2U\mu_1^2\theta_2^2 cos(\phi) + 2U\mu_2^2\theta_1^2 cos(\phi) + U\mu_1\mu_2 cos(\phi) \\
&+ U_{op}\mu_1\mu_2 cos(\theta_2) + U_{op}\mu_2^2 cos(2\theta_1)cos(\theta_2) - U\mu_2^2 sin(2\theta_1)sin(\phi) + U_{op}\mu_2^2 sin(2\theta_1)sin(\theta_2) \\
&- 2U\mu_2^2\theta_1 sin(\phi) + 2U_{op}\mu_2^2\theta_1 sin(\theta_2) - 4U\mu_1\mu_2\theta_1^2 cos(\phi) - 4U\mu_1^2\theta_1\theta_2 cos(\phi) - U_{op}\mu_1\mu_2 cos(2\theta_1)cos(\theta_2) \\
&+ U\mu_1\mu_2 sin(2\theta_1)sin(\phi) - U\mu_1\mu_2 sin(2\theta_2)sin(\phi) - U_{op}\mu_1\mu_2 sin(2\theta_1)sin(\theta_2) \\
&+ U\mu_1^2 cos(2\theta_1)cos(2\theta_2)cos(\phi) + U\mu_1^2 sin(2\theta_1)sin(2\theta_2)cos(\phi) + 2U\mu_1\mu_2\theta_1 sin(\phi) - 2U\mu_1\mu_2\theta_2 sin(\phi) \\
&- 2U_{op}\mu_1\mu_2\theta_1 sin(\theta_2) \ + 2U_{op}\mu_1\mu_2\theta_2 sin(\theta_2) + 4U\mu_1\mu_2\theta_1\theta_2 cos(\phi) \\
&- U\mu_1\mu_2 cos(2\theta_1)cos(2\theta_2)cos(\phi) - U\mu_1\mu_2 sin(2\theta_1)sin(2\theta_2)cos(\phi)) \\
&/(2\mu_1^2\theta_1^2 + 2\mu_1^2\theta_2^2 + 2\mu_2^2\theta_1^2 + \mu_1\mu_2 + \mu_2^2 cos(2\theta_1) + \mu_1^2 cos(2\theta_1 - 2\theta_2) - \mu_1^2 - \mu_2^2 - 4\mu_1\mu_2\theta_1^2 - 4\mu_1^2\theta_1\theta_2 \\
&- \mu_1\mu_2 cos(2\theta_1) + \mu_1\mu_2 cos(2\theta_2) - \mu_1\mu_2 cos(2\theta_1 - 2\theta_2) + 4\mu_1\mu_2\theta_1\theta_2)
\end{aligned} \tag{A6}
$$

$$
B_1 = U sin(\phi) \tag{A7}
$$

$$
\begin{aligned}
C_1 = &(\mu_2(U_{op}\mu_1 sin(\theta_2) - U\mu_2 sin(\phi) + U_{op}\mu_2 sin(\theta_2) - U\mu_1 sin(\phi - 2\theta_1) + U\mu_1 sin(\phi - 2\theta_2) + U\mu_2 sin(\phi - 2\theta_1) \\
&- U_{op}\mu_1 sin(2\theta_1 - \theta_2) + U_{op}\mu_2 sin(2\theta_1 - \theta_2) - 2U\mu_1\theta_1 cos(\phi) + 2U\mu_1\theta_2 cos(\phi) + 2U\mu_2\theta_1 cos(\phi) \\
&+ 2U_{op}\mu_1\theta_1 cos(\theta_2) - 2U_{op}\mu_1\theta_2 cos(\theta_2) - 2U_{op}\mu_2\theta_1 cos(\theta_2))) \\
&/(2\mu_1^2\theta_1^2 + 2\mu_1^2\theta_2^2 + 2\mu_2^2\theta_1^2 + \mu_1\mu_2 + \mu_2^2 cos(2\theta_1) + \mu_1^2 cos(2\theta_1 - 2\theta_2) - \mu_1^2 - \mu_2^2 - 4\mu_1\mu_2\theta_1^2 - 4\mu_1^2\theta_1\theta_2 \\
&- \mu_1\mu_2 cos(2\theta_1) + \mu_1\mu_2 cos(2\theta_2) - \mu_1\mu_2 cos(2\theta_1 - 2\theta_2) + 4\mu_1\mu_2\theta_1\theta_2)
\end{aligned} \tag{A8}
$$

$$
\begin{aligned}
D_1 = &(\mu_2(U\mu_1 cos(\phi - 2\theta_1) - U\mu_1 cos(\phi - 2\theta_2) - U\mu_2 cos(\phi - 2\theta_1) - U_{op}\mu_1 cos(2\theta_1 - \theta_2) + U_{op}\mu_2 cos(2\theta_1 - \theta_2) \\
&+ U\mu_2 cos(\phi) + U_{op}\mu_1 cos(\theta_2) - U_{op}\mu_2 cos(\theta_2) + 2U\mu_1\theta_1 sin(\phi) - 2U\mu_1\theta_2 sin(\phi) - 2U\mu_2\theta_1 sin(\phi) \\
&- 2U_{op}\mu_1\theta_1 sin(\theta_2) + 2U_{op}\mu_1\theta_2 sin(\theta_2) + 2U_{op}\mu_2\theta_1 sin(\theta_2))) \\
&/(2\mu_1^2\theta_1^2 + 2\mu_1^2\theta_2^2 + 2\mu_2^2\theta_1^2 + \mu_1\mu_2 + \mu_2^2 cos(2\theta_1) + \mu_1^2 cos(2\theta_1 - 2\theta_2) - \mu_1^2 - \mu_2^2 - 4\mu_1\mu_2\theta_1^2 - 4\mu_1^2\theta_1\theta_2 \\
&- \mu_1\mu_2 cos(2\theta_1) + \mu_1\mu_2 cos(2\theta_2) - \mu_1\mu_2 cos(2\theta_1 - 2\theta_2) + 4\mu_1\mu_2\theta_1\theta_2)
\end{aligned} \tag{A9}
$$

$$
\begin{aligned}
A_2 = &-((U\mu_1^2 cos(\phi - 2\theta_1 + 2\theta_2))/2 - U_{op}\mu_2^2 cos(\theta_2) - (U\mu_1^2 cos(\phi))/2 + (U\mu_1^2 cos(\phi - 2\theta_1))/2 - (U\mu_1^2 cos(\phi - 2\theta_2))/2 \\
&+ (U_{op}\mu_2^2 cos(2\theta_1 + \theta_2))/2 + (U_{op}\mu_2^2 cos(2\theta_1 - \theta_2))/2 + U\mu_1^2\theta_1 sin(\phi - 2\theta_2) - U\mu_1^2\theta_2 sin(\phi - 2\theta_1) + 2U\mu_1^2\theta_2^2 cos(\phi) \\
&+ 2U_{op}\mu_1^2\theta_1^2 cos(\theta_2) + 2U_{op}\mu_2^2\theta_1^2 cos(\theta_2) + (U\mu_1\mu_2 cos(\phi))/2 + U_{op}\mu_1\mu_2 cos(\theta_2) - (U\mu_1\mu_2 cos(\phi - 2\theta_1 + 2\theta_2))/2 \\
&- U_{op}\mu_1^2\theta_2 sin(2\theta_1 - \theta_2) - (U\mu_1\mu_2 cos(\phi - 2\theta_1))/2 + (U\mu_1\mu_2 cos(\phi + 2\theta_2))/2 - (U_{op}\mu_1\mu_2 cos(2\theta_1 + \theta_2))/2 \\
&+ U\mu_1^2\theta_1 sin(\phi) - U\mu_1^2\theta_2 sin(\phi) + U_{op}\mu_1^2\theta_2 sin(\theta_2) - (U_{op}\mu_1\mu_2 cos(2\theta_1 - \theta_2))/2 - U\mu_1\mu_2\theta_1 sin(\phi - 2\theta_2) \\
&+ U\mu_1\mu_2\theta_2 sin(\phi - 2\theta_1) - 4U_{op}\mu_1\mu_2\theta_1^2 cos(\theta_2) - 2U\mu_1^2\theta_1\theta_2 cos(\phi) - 2U_{op}\mu_1^2\theta_1\theta_2 cos(\theta_2) + U_{op}\mu_1\mu_2\theta_2 sin(2\theta_1 - \theta_2) \\
&- U\mu_1\mu_2\theta_1 sin(\phi) - U\mu_1\mu_2\theta_2 sin(\phi) + U_{op}\mu_1\mu_2\theta_2 sin(\theta_2) + 2U\mu_1\mu_2\theta_1\theta_2 cos(\phi) + 2U_{op}\mu_1\mu_2\theta_1\theta_2 cos(\theta_2)) \\
&/(2\mu_1^2\theta_1^2 + 2\mu_1^2\theta_2^2 + 2\mu_2^2\theta_1^2 + \mu_1\mu_2 + \mu_2^2 cos(2\theta_1) + \mu_1^2 cos(2\theta_1 - 2\theta_2) - \mu_1^2 - \mu_2^2 - 4\mu_1\mu_2\theta_1^2 - 4\mu_1^2\theta_1\theta_2 \\
&- \mu_1\mu_2 cos(2\theta_1) + \mu_1\mu_2 cos(2\theta_2) - \mu_1\mu_2 cos(2\theta_1 - 2\theta_2) + 4\mu_1\mu_2\theta_1\theta_2)
\end{aligned}
$$

https://doi.org/10.5194/egusphere-2025-2909
Preprint. Discussion started: 12 August 2025

(A10)

$$B_2 = ((U\mu_1^2 sin(\phi - 2\theta_1 + 2\theta_2))/2 - U_{op}\mu_2^2 sin(\theta_2) - (U\mu_1^2 sin(\phi))/2 - (U\mu_1^2 sin(\phi - 2\theta_1))/2 + (U\mu_1^2 sin(\phi - 2\theta_2))/2$$
$$+ (U_{op}\mu_2^2 sin(2\theta_1 + \theta_2))/2 - (U_{op}\mu_2^2 sin(2\theta_1 - \theta_2))/2 + (U_{op}\mu_1\mu_2 sin(2\theta_1 - \theta_2))/2 + 2U\mu_1^2\theta_2^2 sin(\phi) + 2U_{op}\mu_1^2\theta_1^2 sin(\theta_2)$$
$$+ 2U_{op}\mu_2^2\theta_1^2 sin(\theta_2) + U_{op}\mu_1^2\theta_2 cos(2\theta_1 - \theta_2) - (U\mu_1\mu_2 sin(\phi))/2 + U_{op}\mu_1\mu_2 sin(\theta_2) - (U\mu_1\mu_2 sin(\phi - 2\theta_1 + 2\theta_2))/2$$
$$+ (U\mu_1\mu_2 sin(\phi - 2\theta_1))/2 + (U\mu_1\mu_2 sin(\phi + 2\theta_2))/2 - (U_{op}\mu_1\mu_2 sin(2\theta_1 + \theta_2))/2 - U\mu_1^2\theta_1 cos(\phi) + U\mu_1^2\theta_2 cos(\phi)$$
$$- U_{op}\mu_1^2\theta_2 cos(\theta_2) + U\mu_1^2\theta_1 cos(\phi - 2\theta_2) - U\mu_1^2\theta_2 cos(\phi - 2\theta_1) - U\mu_1\mu_2\theta_1 cos(\phi - 2\theta_2) + U\mu_1\mu_2\theta_2 cos(\phi - 2\theta_1)$$
$$- 4U_{op}\mu_1\mu_2\theta_1^2 sin(\theta_2) - 2U\mu_1^2\theta_1\theta_2 sin(\phi) - 2U_{op}\mu_1^2\theta_1\theta_2 sin(\theta_2) - U_{op}\mu_1\mu_2\theta_2 cos(2\theta_1 - \theta_2) + U\mu_1\mu_2\theta_1 cos(\phi)$$
$$- U\mu_1\mu_2\theta_2 cos(\phi) + U_{op}\mu_1\mu_2\theta_2 cos(\theta_2) + 2U\mu_1\mu_2\theta_1\theta_2 sin(\phi) + 2U_{op}\mu_1\mu_2\theta_1\theta_2 sin(\theta_2))$$
$$/(2\mu_1^2\theta_1^2 + 2\mu_1^2\theta_2^2 + 2\mu_2^2\theta_1^2 + \mu_1\mu_2 + \mu_2^2 cos(2\theta_1) + \mu_1^2 cos(2\theta_1 - 2\theta_2) - \mu_1^2 - \mu_2^2 - 4\mu_1\mu_2\theta_1^2 - 4\mu_1^2\theta_1\theta_2$$
$$- \mu_1\mu_2 cos(2\theta_1) + \mu_1\mu_2 cos(2\theta_2) - \mu_1\mu_2 cos(2\theta_1 - 2\theta_2) + 4\mu_1\mu_2\theta_1\theta_2)$$

(A11)

$$C_2 = (\mu_1(U_{op}\mu_1 sin(\theta_2) - U\mu_2 sin(\phi) + U_{op}\mu_2 sin(\theta_2) - U\mu_1 sin(\phi - 2\theta_1) + U\mu_1 sin(\phi - 2\theta_2) + U\mu_2 sin(\phi - 2\theta_1)$$
$$- U_{op}\mu_1 sin(2\theta_1 - \theta_2) + U_{op}\mu_2 sin(2\theta_1 - \theta_2) - 2U\mu_1\theta_1 cos(\phi) + 2U\mu_1\theta_2 cos(\phi) + 2U\mu_2\theta_1 cos(\phi)$$
$$+ 2U_{op}\mu_1\theta_1 cos(\theta_2) - 2U_{op}\mu_1\theta_2 cos(\theta_2) - 2U_{op}\mu_2\theta_1 cos(\theta_2)))$$
$$/(2\mu_1^2\theta_1^2 + 2\mu_1^2\theta_2^2 + 2\mu_2^2\theta_1^2 + \mu_1\mu_2 + \mu_2^2 cos(2\theta_1) + \mu_1^2 cos(2\theta_1 - 2\theta_2) - \mu_1^2 - \mu_2^2 - 4\mu_1\mu_2\theta_1^2$$
$$- 4\mu_1^2\theta_1\theta_2 - \mu_1\mu_2 cos(2\theta_1) + \mu_1\mu_2 cos(2\theta_2) - \mu_1\mu_2 cos(2\theta_1 - 2\theta_2) + 4\mu_1\mu_2\theta_1\theta_2) \quad \text{(A12)}$$

$$D_2 = (\mu_1(U\mu_1 cos(\phi - 2\theta_1) - U\mu_1 cos(\phi - 2\theta_2) - U\mu_2 cos(\phi - 2\theta_1) - U_{op}\mu_1 cos(2\theta_1 - \theta_2) + U_{op}\mu_2 cos(2\theta_1 - \theta_2)$$
$$+ U\mu_2 cos(\phi) + U_{op}\mu_1 cos(\theta_2) - U_{op}\mu_2 cos(\theta_2) + 2U\mu_1\theta_1 sin(\phi) - 2U\mu_1\theta_2 sin(\phi) - 2U\mu_2\theta_1 sin(\phi)$$
$$- 2U_{op}\mu_1\theta_1 sin(\theta_2) + 2U_{op}\mu_1\theta_2 sin(\theta_2) + 2U_{op}\mu_2\theta_1 sin(\theta_2)))$$
$$/(2\mu_1^2\theta_1^2 + 2\mu_1^2\theta_2^2 + 2\mu_2^2\theta_1^2 + \mu_1\mu_2 + \mu_2^2 cos(2\theta_1) + \mu_1^2 cos(2\theta_1 - 2\theta_2) - \mu_1^2 - \mu_2^2 - 4\mu_1\mu_2\theta_1^2 - 4\mu_1^2\theta_1\theta_2$$
$$- \mu_1\mu_2 cos(2\theta_1) + \mu_1\mu_2 cos(2\theta_2) - \mu_1\mu_2 cos(2\theta_1 - 2\theta_2) + 4\mu_1\mu_2\theta_1\theta_2) \quad \text{(A13)}$$

Substituting the expressions of these eight constants in Eqs. 12, and 11, the two stream functions (ψ_1 and ψ_2) are calculated. These two stream functions (Eq.11) are then utilized to find the velocity field in the wedge as well as the overriding plate.

Author contributions. AP conducted the theoretical analysis, performed the laboratory experiments, and prepared the initial draft. NM conceptualized the research idea, supervised the methodologies, and revised the initial draft.

Competing interests. The contact author has declared that none of the authors has any competing interests.

https://doi.org/10.5194/egusphere-2025-2909
Preprint. Discussion started: 12 August 2025

Acknowledgements. This work has been supported by the DST-SERB through J. C. Bose fellowship (JBR/2022/000003) to NM. AP gratefully acknowledges CSIR, India for awarding him a Senior Research Fellowship grant (09/096(1029)/2020-EMR-I).

https://doi.org/10.5194/egusphere-2025-2909
Preprint. Discussion started: 12 August 2025

References

Abers, G. A., Van Keken, P. E., and Hacker, B. R.: The cold and relatively dry nature of mantle forearcs in subduction zones, Nature Geoscience 2017 10:5, 10, 333–337, https://doi.org/10.1038/ngeo2922, 2017.

Agard, P., Jolivet, L., and Goffé, B.: Tectonometamorphic evolution of the Schistes Lustres Complex; implications for the exhumation of HP and UHP rocks in the Western Alps, Bulletin de la Société Géologique de France, 172, 617–636, https://doi.org/10.2113/172.5.617, 2001.

Agard, P., Monié, P., Jolivet, L., and Goffé, B.: Exhumation of the Schistes Lustrés complex: in situ laser probe 40Ar/39Ar constraints and implications for the Western Alps, Journal of Metamorphic Geology, 20, 599–618, https://doi.org/10.1046/J.1525-1314.2002.00391.X, 2002.

Agard, P., Yamato, P., Jolivet, L., and Burov, E.: Exhumation of oceanic blueschists and eclogites in subduction zones: Timing and mechanisms, Earth-Science Reviews, 92, 53–79, https://doi.org/10.1016/J.EARSCIREV.2008.11.002, 2009.

Agard, P., Plunder, A., Angiboust, S., Bonnet, G., and Ruh, J.: The subduction plate interface: rock record and mechanical coupling (from long to short timescales), Lithos, 320-321, 537–566, https://doi.org/10.1016/J.LITHOS.2018.09.029, 2018.

Allemand, P. and Lardeaux, J. M.: Strain partitioning and metamorphism in a deformable orogenic wedge: Application to the Alpine belt, Tectonophysics, 280, 157–169, https://doi.org/10.1016/S0040-1951(97)00136-4, 1997.

Anderson, D. M. and Davis, S. H.: Two-fluid viscous flow in a corner, Journal of Fluid Mechanics, 257, 1–31, https://doi.org/10.1017/S0022112093002976, 1993.

Angiboust, S., Wolf, S., Burov, E., Agard, P., and Yamato, P.: Effect of fluid circulation on subduction interface tectonic processes: Insights from thermo-mechanical numerical modelling, Earth and Planetary Science Letters, 357, 238–248, 2012.

Angiboust, S., Menant, A., Gerya, T., and Oncken, O.: The rise and demise of deep accretionary wedges: A long-term field and numerical modeling perspective, Geosphere, 18, 69–103, https://doi.org/10.1130/GES02392.1, 2022.

Batchelor, G. K.: An Introduction to Fluid Dynamics, Cambridge University Press, 1967.

Beaumont, C., Ellis, S., and Pfiffner, A.: Dynamics of sediment subduction-accretion at convergent margins: Short-term modes, long-term deformation, and tectonic implications, Journal of Geophysical Research: Solid Earth, 104, 17 573–17 601, https://doi.org/10.1029/1999JB900136, 1999.

Beaumont, C., Jamieson, R. A., Nguyen, M. H., and Lee, B.: Himalayan tectonics explained by extrusion of a low-viscosity crustal channel coupled to focused surface denudation, Nature, 414, 738–742, https://doi.org/10.1038/414738A, 2001.

Beaumont, C., Jamieson, R., Butler, J., and Warren, C.: Crustal structure: A key constraint on the mechanism of ultra-high-pressure rock exhumation, Earth and Planetary Science Letters, 287, 116–129, 2009.

Behr, W. M. and Becker, T. W.: Sediment control on subduction plate speeds, Earth and Planetary Science Letters, 502, 166–173, https://doi.org/10.1016/J.EPSL.2018.08.057, 2018.

Behr, W. M., Holt, A. F., Becker, T. W., and Faccenna, C.: The effects of plate interface rheology on subduction kinematics and dynamics, Geophysical Journal International, 230, 796–812, https://doi.org/10.1093/GJI/GGAC075, 2022.

Bento dos Santos, T., Rodrigues, J. F., Castro, P., Cotrim, B., Pereira, I., Ferreira, J. A., Meireles, C., Ferreira, N., Ferreira, P., Ribeiro, A., and Guimarães, F.: Exhumation of an anatectic complex by channel flow and extrusion tectonics: structural and metamorphic evidence from the Porto–Viseu Metamorphic Belt, Central-Iberian Zone, International Journal of Earth Sciences, 110, 2179–2201, https://doi.org/10.1007/S00531-021-02067-Z/FIGURES/11, 2021.

https://doi.org/10.5194/egusphere-2025-2909
Preprint. Discussion started: 12 August 2025

Bezada, M. J., Humphreys, E. D., Toomey, D. R., Harnafi, M., Dávila, J. M., and Gallart, J.: Evidence for slab rollback in westernmost Mediterranean from improved upper mantle imaging, Earth and Planetary Science Letters, 368, 51–60, https://doi.org/10.1016/J.EPSL.2013.02.024, 2013.

Brandon, M. T., Roden-Tice, M. K., Garver, J. I., Brandon, M. T., Roden-Tice, M. K., and Garver, J. I.: Late Cenozoic exhumation of the Cascadia accretionary wedge in the Olympic Mountains, northwest Washington State, GSAB, 110, 985–1009, https://doi.org/10.1130/0016-7606(1998)110, 1998.

Brun, J. P. and Faccenna, C.: Exhumation of high-pressure rocks driven by slab rollback, Earth and Planetary Science Letters, 272, 1–7, https://doi.org/10.1016/J.EPSL.2008.02.038, 2008.

Buiter, S. J.: A review of brittle compressional wedge models, Tectonophysics, 530, 1–17, 2012.

Buiter, S. J., Govers, R., and Wortel, M. J.: A modelling study of vertical surface displacements at convergent plate margins, Geophysical Journal International, 147, 415–427, https://doi.org/10.1046/J.1365-246X.2001.00545.X/2/147-2-415-FIG010.JPEG, 2001.

Burov, E. and Yamato, P.: Continental plate collision, P–T–t–z conditions and unstable vs. stable plate dynamics: Insights from thermomechanical modelling, Lithos, 103, 178–204, https://doi.org/10.1016/J.LITHOS.2007.09.014, 2008.

Burov, E., Jolivet, L., Le Pourhiet, L., and Poliakov, A.: A thermomechanical model of exhumation of high pressure (HP) and ultra-high pressure (UHP) metamorphic rocks in Alpine-type collision belts, Tectonophysics, 342, 113–136, https://doi.org/10.1016/S0040-1951(01)00158-5, 2001.

Butler, J. P., Beaumont, C., and Jamieson, R. A.: Crustal emplacement of exhuming (ultra)high-pressure rocks: Will that be pro- or retro-side?, Geology, 39, 635–638, https://doi.org/10.1130/G32166.1, 2011.

Candioti, L. G., Duretz, T., Moulas, E., and Schmalholz, S. M.: Buoyancy versus shear forces in building orogenic wedges, Solid Earth, 12, 1749–1775, https://doi.org/10.5194/SE-12-1749-2021, 2021.

Cawood, P. A., Kröner, A., Collins, W. J., Kusky, T. M., Mooney, W. D., and Windley, B. F.: Accretionary orogens through Earth history, Geological Society Special Publication, 318, 1–36, https://doi.org/10.1144/SP318.1, 2009.

Cerpa, N. G. and Arcay, D.: Overriding Plate Velocity Control on Surface Topography in 2-D Models of Subduction Zones, Geochemistry, Geophysics, Geosystems, 21, e2019GC008 900, https://doi.org/10.1029/2019GC008900, 2020.

Chattopadhyay, A. and Mandal, N.: Progressive changes in strain patterns and fold styles in a deforming ductile orogenic wedge: an experimental study, Journal of Geodynamics, 33, 353–376, https://doi.org/10.1016/S0264-3707(01)00079-5, 2002.

Chemenda, A., Lallemand, S., and Bokun, A.: Strain partitioning and interplate friction in oblique subduction zones: Constraints provided by experimental modeling, Journal of Geophysical Research: Solid Earth, 105, 5567 – 5581, https://doi.org/10.1029/1999jb900332, 2000.

Chemenda, A. I., Mattauer, M., Malavieille, J., and Bokun, A. N.: A mechanism for syn-collisional rock exhumation and associated normal faulting: Results from physical modelling, Earth and Planetary Science Letters, 132, 225–232, https://doi.org/10.1016/0012-821X(95)00042-B, 1995.

Chen, Z., Schellart, W. P., Duarte, J. C., and Strak, V.: Topography of the Overriding Plate During Progressive Subduction: A Dynamic Model to Explain Forearc Subsidence, Geophysical Research Letters, 44, 9632–9643, https://doi.org/10.1002/2017GL074672;SUBPAGE:STRING:FULL, 2017.

Clift, P. and Vannucchi, P.: Controls on tectonic accretion versus erosion in subduction zones: Implications for the origin and recycling of the continental crust, Reviews of Geophysics, 42, https://doi.org/10.1029/2003RG000127, 2004.

https://doi.org/10.5194/egusphere-2025-2909
Preprint. Discussion started: 12 August 2025

Cloos, M.: Flow melanges: Numerical modeling and geologic constraints on their origin in the Franciscan subduction complex, California | GSA Bulletin | GeoScienceWorld, https://pubs.geoscienceworld.org/gsa/gsabulletin/article-abstract/93/4/330/202762/Flow-melanges-Numerical-modeling-and-geologic?redirectedFrom=fulltext, 1982.

Cloos, M. and Shreve, R. L.: Subduction-channel model of prism accretion, melange formation, sediment subduction, and subduction erosion at convergent plate margins: 2. Implications and discussion, Pure and Applied Geophysics PAGEOPH, 128, 501–545, https://doi.org/10.1007/BF00874549/METRICS, 1988.

Dahlen, F. A.: Critical taper model of fold-and-thrust belts and accretionary wedges, Annual Review of Earth Planetary Sciences, 18, 55–99, https://doi.org/10.1146/ANNUREV.EA.18.050190.000415, 1990.

Dahlen, F. A., Suppe, J., and Davis, D.: Mechanics of fold-and-thrust belts and accretionary wedges: Cohesive Coulomb Theory, Journal of Geophysical Research: Solid Earth, 89, 10 087–10 101, https://doi.org/10.1029/JB089IB12P10087, 1984.

Dasgupta, R. and Mandal, N.: Surface topography of the overriding plates in bi-vergent subduction systems: A mechanical model, Tectonophysics, 746, 280–295, https://doi.org/10.1016/J.TECTO.2017.08.008, 2018.

Deville, E.: Dynamics of Brittle-Viscous Accretionary Wedges as Revealed by Geophysical and Drilling Data and Analog Modeling of the Barbados Prism, Tectonics, 42, e2023TC007 851, https://doi.org/10.1029/2023TC007851;WGROUP:STRING:PUBLICATION, 2023.

Di Giuseppe, E., Faccenna, C., Funiciello, F., van Hunen, J., and Giardini, D.: On the relation between trench migration, seafloor age, and the strength of the subducting lithosphere, Lithosphere, 1, 121–128, https://doi.org/10.1130/L26.1, 2009.

Ducharme, T. A., Schneider, D. A., Grasemann, B., and Klonowska, I.: Stretched Thin: Oligocene Extrusion and Ductile Thinning of the Basal Unit Along the Evia Shear Zone, NW Cyclades, Greece, Tectonics, 41, e2022TC007 561, https://doi.org/10.1029/2022TC007561;WGROUP:STRING:PUBLICATION, 2022.

England, P. C. and Holland, T. J.: Archimedes and the Tauern eclogites: the role of buoyancy in the preservation of exotic eclogite blocks, Earth and Planetary Science Letters, 44, 287–294, https://doi.org/10.1016/0012-821X(79)90177-8, 1979.

England, P. C. and Richardson, S. W.: The influence of erosion upon the mineral fades of rocks from different metamorphic environments, Journal of the Geological Society, 134, 201–213, https://doi.org/10.1144/GSJGS.134.2.0201, 1977.

Ernst, W.: Metamorphism of Franciscan tectonostratigraphic assemblage, Pacheco Pass area, east-central Diablo Range, California coast ranges, Geological Society of America Bulletin, 105, 618–636, 1993.

Ernst, W. G., Ernst, and G., W.: Tectonic history of subduction zones inferred from retrograde blueschist P-T paths, Geo, 16, 1081, https://doi.org/10.1130/0091-7613(1988)016, 1988.

Ernst, W. G., Maruyama, S., and Wallis, S.: Buoyancy-driven, rapid exhumation of ultrahigh-pressure metamorphosed continental crust, Proceedings of the National Academy of Sciences of the United States of America, 94, 9532–9537, https://doi.org/10.1073/PNAS.94.18.9532/ASSET/7791F8EE-966C-49A5-96CF-34E9069F04D9/ASSETS/GRAPHIC/PQ1771997003.JPEG, 1997.

Federico, L., Capponi, G., Crispini, L., Scambelluri, M., and Villa, I. M.: 39Ar / 40Ar dating of high-pressure rocks from the Ligurian Alps: Evidence for a continuous subduction–exhumation cycle, Earth and Planetary Science Letters, 240, 668–680, https://doi.org/10.1016/J.EPSL.2005.09.062, 2005.

Feehan, J. G. and Brandon, M. T.: Contribution of ductile flow to exhumation of low-temperature, high-pressure metamorphic rocks: San Juan-Cascade nappes, NW Washington State, Journal of Geophysical Research: Solid Earth, 104, 10 883–10 902, https://doi.org/10.1029/1998JB900054, 1999.

https://doi.org/10.5194/egusphere-2025-2909
Preprint. Discussion started: 12 August 2025

Fernández-Blanco, D., Mannu, U., Bertotti, G., and Willett, S. D.: Forearc high uplift by lower crustal flow during growth of the Cyprus-Anatolian margin, Earth and Planetary Science Letters, 544, 116 314, https://doi.org/10.1016/J.EPSL.2020.116314, 2020.

Gerya, T.: Tectonic overpressure and underpressure in lithospheric tectonics and metamorphism, Journal of Metamorphic Geology, 33, 785–800, https://doi.org/10.1111/JMG.12144, 2015.

Gerya, T. V., Stöckhert, B., and Perchuk, A. L.: Exhumation of high-pressure metamorphic rocks in a subduction channel: A numerical simulation, Tectonics, 21, 6–1, https://doi.org/10.1029/2002TC001406, 2002.

Glodny, J., Lohrmann, J., Echtler, H., Gräfe, K., Seifert, W., Collao, S., and Figueroa, O.: Internal dynamics of a paleoaccretionary wedge: insights from combined isotope tectonochronology and sandbox modelling of the South-Central Chilean forearc, Earth and Planetary Science Letters, 231, 23–39, https://doi.org/10.1016/J.EPSL.2004.12.014, 2005.

Godin, L., Grujic, D., Law, R. D., and Searle, M. P.: Channel flow, ductile extrusion and exhumation in continental collision zones: An introduction, Geological Society Special Publication, 268, 1–23, https://doi.org/10.1144/GSL.SP.2006.268.01.01, 2006.

Grujic, D.: Channel flow and continental collision tectonics: An overview, Geological Society Special Publication, 268, 25–37, https://doi.org/10.1144/GSL.SP.2006.268.01.02, 2006.

Grujic, D., Hollister, L. S., and Parrish, R. R.: Himalayan metamorphic sequence as an orogenic channel: insight from Bhutan, Earth and Planetary Science Letters, 198, 177–191, https://doi.org/10.1016/S0012-821X(02)00482-X, 2002.

Guillaume, B., Martinod, J., and Espurt, N.: Variations of slab dip and overriding plate tectonics during subduction: Insights from analogue modelling, Tectonophysics, 463, 167–174, https://doi.org/10.1016/J.TECTO.2008.09.043, 2009.

Hampel, A. and Pfiffner, A.: Relative importance of trenchward upper plate motion and friction along the plate interface for the topographic evolution of subduction-related mountain belts, Geological Society Special Publication, 253, 105–115, https://doi.org/10.1144/GSL.SP.2006.253.01.05;PAGEGROUP:STRING:PUBLICATION, 2006.

Hu, J., Liu, L., and Gurnis, M.: Southward expanding plate coupling due to variation in sediment subduction as a cause of Andean growth, Nature Communications 2021 12:1, 12, 1–9, https://doi.org/10.1038/s41467-021-27518-8, 2021.

Husson, L., Brun, J. P., Yamato, P., and Faccenna, C.: Episodic slab rollback fosters exhumation of HP-UHP rocks, Geophysical Journal International, 179, 1292–1300, https://doi.org/10.1111/J.1365-246X.2009.04372.X/3/179-3-1292-FIG007.JPEG, 2009.

Iwamori, H.: Viscous flow and deformation of regional metamorphic belts at convergent plate boundaries, Journal of Geophysical Research: Solid Earth, 108, https://doi.org/10.1029/2002JB001808, 2003.

Jarrard, R. D.: Relations among subduction parameters, Reviews of Geophysics, 24, 217–284, https://doi.org/10.1029/RG024I002P00217, 1986.

Lamb, S. and Davis, P.: Cenozoic climate change as a possible cause for the rise of the Andes, Nature 2003 425:6960, 425, 792–797, https://doi.org/10.1038/nature02049, 2003.

Lee, C. and Kim, Y. H.: Understanding subduction infancy to mature subduction in Southwest Japan via the self-consistent formation of a weak slab interface, Scientific Reports 2023 13:1, 13, 1–14, https://doi.org/10.1038/s41598-023-48746-6, 2023.

Li, Z. H., Gerya, T. V., and Burg, J. P.: Influence of tectonic overpressure on P–T paths of HP–UHP rocks in continental collision zones: thermomechanical modelling, Journal of Metamorphic Geology, 28, 227–247, https://doi.org/10.1111/J.1525-1314.2009.00864.X, 2010.

Luján, M., Rossetti, F., Storti, F., Ranalli, G., and A. Socquet: Flow trajectories in analogue viscous orogenic wedges: Insights on natural orogens, Tectonophysics, 484, 119–126, https://doi.org/10.1016/J.TECTO.2009.09.009, 2010.

Maiti, G., Mandal, N., and Misra, S.: Insights into the dynamics of an orogenic wedge from lubrication theory: Implications for the Himalayan tectonics, Tectonophysics, 776, 228 335, 2020.

https://doi.org/10.5194/egusphere-2025-2909
Preprint. Discussion started: 12 August 2025

Mancktelow, N. S.: Nonlithostatic pressure during sediment subduction and the development and exhumation of high pressure metamorphic rocks, Journal of Geophysical Research: Solid Earth, 100, 571–583, https://doi.org/10.1029/94JB02158, 1995.

Mannu, U., Ueda, K., Willett, S. D., Gerya, T. V., and Strasser, M.: Impact of sedimentation on evolution of accretionary wedges: Insights from high-resolution thermomechanical modeling, Tectonics, 35, 2828–2846, https://doi.org/10.1002/2016TC004239, 2016.

Marques, F. O., Mandal, N., Ghosh, S., Ranalli, G., and Bose, S.: Channel flow, tectonic overpressure, and exhumation of high-pressure rocks in the greater himalayas, Solid Earth, 9, 1061–1078, https://doi.org/10.5194/SE-9-1061-2018, 2018.

McCaffrey, R.: Oblique plate convergence, slip vectors, and forearc deformation, Journal of Geophysical Research: Solid Earth, 97, 8905–8915, https://doi.org/10.1029/92JB00483, 1992.

Means, W. D., Hobbs, B. E., Lister, G. S., and Williams, P. F.: Vorticity and non-coaxiality in progressive deformations, Journal of Structural Geology, 2, 371–378, https://doi.org/10.1016/0191-8141(80)90024-3, 1980.

Moulas, E., Brandon, M. T., Vaughan Hammon, J. D., and Schmalholz, S. M.: On backflow associated with oceanic and continental subduction, Geophysical Journal International, 227, 576–590, https://doi.org/10.1093/GJI/GGAB246, 2021.

Muñoz-Montecinos, J., Angiboust, S., Cambeses, A., and García-Casco, A.: Multiple veining in a paleo–accretionary wedge: The metamorphic rock record of prograde dehydration and transient high pore-fluid pressures along the subduction interface (Western Series, central Chile), Geosphere, 16, 765–786, 2020.

Nakakuki, T. and Mura, E.: Dynamics of slab rollback and induced back-arc basin formation, Earth and Planetary Science Letters, 361, 287–297, https://doi.org/10.1016/J.EPSL.2012.10.031, 2013.

Nettesheim, M., Ehlers, T. A., Whipp, D. M., and Koptev, A.: The influence of upper-plate advance and erosion on overriding plate deformation in orogen syntaxes, Solid Earth, 9, 1207–1224, 2018.

Osozawa, S. and Wakabayashi, J.: Late stage exhumation of HP metamorphic rocks, progressive localization of strain, and changes in transport direction, Sambagawa belt, Japan, Journal of Structural Geology, 75, 1–16, https://doi.org/10.1016/J.JSG.2015.03.006, 2015.

Pavlis, T. L. and Bruhn, R. L.: Deep-seated flow as a mechanism for the uplift of broad forearc ridges and its role in the exposure of high P/T metamorphic terranes, Tectonics, 2, 473–497, https://doi.org/10.1029/TC002I005P00473, 1983.

Petrini, K. and Podladchikov, Y.: Lithospheric pressure-depth relationship in compressive regions of thickened crust, Journal of Metamorphic Geology, 18, 67–77, https://doi.org/10.1046/J.1525-1314.2000.00240.X;PAGEGROUP:STRING:PUBLICATION, 2000.

Platt, J.: Dynamics of orogenic wedges and the uplift of high-pressure metamorphic rocks | GSA Bulletin | GeoScienceWorld, https://pubs.geoscienceworld.org/gsa/gsabulletin/article-abstract/97/9/1037/203199/Dynamics-of-orogenic-wedges-and-the-uplift-of-high?redirectedFrom=fulltext, 1986.

Platt, J. P.: Exhumation of high-pressure rocks: a review of concepts and processes, Terra Nova, 5, 119–133, https://doi.org/10.1111/J.1365-3121.1993.TB00237.X, 1993.

Pusok, A. E., Stegman, D. R., and Kerr, M.: The effect of low-viscosity sediments on the dynamics and accretionary style of subduction margins, Solid Earth, 13, 1455–1473, https://doi.org/10.5194/SE-13-1455-2022, 2022.

Raimbourg, H. and Kimura, G.: Non-lithostatic pressure in subduction zones, Earth and Planetary Science Letters, 274, 414–422, https://doi.org/10.1016/J.EPSL.2008.07.037, 2008.

Ranalli, G.: Rheology of the earth, Chapman Hall, ISBN 9780412546709, https://link.springer.com/book/9780412546709, 1995.

Reuber, G., Kaus, B. J., Schmalholz, S. M., and White, R. W.: Nonlithostatic pressure during subduction and collision and the formation of (ultra)high-pressure rocks, Geology, 44, 343–346, https://doi.org/10.1130/G37595.1, 2016.

https://doi.org/10.5194/egusphere-2025-2909
Preprint. Discussion started: 12 August 2025

Ribe, N. M.: Bending mechanics and mode selection in free subduction: A thin-sheet analysis, Geophysical Journal International, 180, 559–576, https://doi.org/10.1111/J.1365-246X.2009.04460.X/3/M_180-2-559-EQ063.JPEG, 2010.

Ribe, N. M.: Analytical Approaches to Mantle Dynamics, Treatise on Geophysics: Second Edition, 7, 145–196, https://doi.org/10.1016/B978-0-444-53802-4.00129-9, 2015.

Ribe, N. M.: Theoretical Mantle Dynamics, Theoretical Mantle Dynamics, pp. 1–314, https://doi.org/10.1017/9781316795897, 2018.

Richter, P. P., Ring, U., Willner, A. P., and Leiss, B.: Structural contacts in subduction complexes and their tectonic significance: The Late Palaeozoic coastal accretionary wedge of central Chile, Journal of the Geological Society, 164, 203–214, https://doi.org/10.1144/0016-76492005-181/ASSET/DF2632F7-B4CF-4F23-A4AD-772A1B78505C/ASSETS/GRAPHIC/05181-10.JPEG, 2007.

Ring, U. and Brandon, M. T.: Exhumation settings, part I: Relatively simple cases, International Geology Review, 50, 97–120, https://doi.org/10.2747/0020-6814.50.2.97;WGROUP:STRING:PUBLICATION, 2008.

Ring, U., Brandon, M. T., Willett, S. D., and Lister, G. S.: Exhumation processes, Geological Society Special Publication, 154, 1–27, https://doi.org/10.1144/GSL.SP.1999.154.01.01, 1999.

Ring, U., Will, T., Glodny, J., Kumerics, C., Gessner, K., Thomson, S., Güngör, T., Monié, P., Okrusch, M., and Drüppel, K.: Early exhumation of high-pressure rocks in extrusion wedges: Cycladic blueschist unit in the eastern Aegean, Greece, and Turkey, Tectonics, 26, https://doi.org/10.1029/2005TC001872, 2007.

Ring, U., Pantazides, H., Glodny, J., and Skelton, A.: Forced Return Flow Deep in the Subduction Channel, Syros, Greece, Tectonics, 39, e2019TC005 768, https://doi.org/10.1029/2019TC005768, 2020.

Rubatto, D. and Hermann, J.: Exhumation as fast as subduction?, Geo, 29, 3, https://doi.org/10.1130/0091-7613(2001)029, 2001.

Sanhueza, J., Yáñez, G., Barra, F., Maringue, J., Figueroa, R., and Sáez, E.: Rheological, petrophysical and geometrical constraints of a subduction channel from a numerical model perspective: Insights from La Cabaña Paleozoic peridotites, Coastal Cordillera of south-central Chile, Journal of South American Earth Sciences, 114, 103 706, 2022.

Schellart, W. P.: Kinematics and flow patterns in deep mantle and upper mantle subduction models: Influence of the mantle depth and slab to mantle viscosity ratio, Geochemistry, Geophysics, Geosystems, 9, https://doi.org/10.1029/2007GC001656, 2008.

Schellart, W. P.: Subduction dynamics and overriding plate deformation, Earth-Science Reviews, 253, 104 755, https://doi.org/10.1016/J.EARSCIREV.2024.104755, 2024.

Schmalholz, S. M. and Podladchikov, Y. Y.: Tectonic overpressure in weak crustal-scale shear zones and implications for the exhumation of high-pressure rocks, Geophysical Research Letters, 40, 1984–1988, https://doi.org/10.1002/GRL.50417;PAGEGROUP:STRING:PUBLICATION, 2013.

Schmalholz, S. M., Medvedev, S., Lechmann, S. M., and Podladchikov, Y.: Relationship between tectonic overpressure, deviatoric stress, driving force, isostasy and gravitational potential energy, Geophysical Journal International, 197, 680–696, https://doi.org/10.1093/GJI/GGU040, 2014.

Schwartz, S., Allemand, P., and Guillot, S.: Numerical model of the effect of serpentinites on the exhumation of eclogitic rocks: insights from the Monviso ophiolitic massif (Western Alps), Tectonophysics, 342, 193–206, 2001.

Searle, M. P.: Mountain Building, Tectonic Evolution, Rheology, and Crustal Flow in the Himalaya, Karakoram, and Tibet, Treatise on Geophysics: Second Edition, 6, 469–511, https://doi.org/10.1016/B978-0-444-53802-4.00121-4, 2015.

Shijie Zhong and Gurnis, M.: Controls on trench topography from dynamic models of subducted slabs, Journal of Geophysical Research: Solid Earth, 99, 15 683–15 695, https://doi.org/10.1029/94JB00809, 1994.

https://doi.org/10.5194/egusphere-2025-2909
Preprint. Discussion started: 12 August 2025

Shreve, R. L. and Cloos, M.: Dynamics of sediment subduction, melange formation, and prism accretion, Journal of Geophysical Research: Solid Earth, 91, 10 229–10 245, https://doi.org/10.1029/JB091IB10P10229, 1986.

Simpson, G. D.: Formation of accretionary prisms influenced by sediment subduction and supplied by sediments from adjacent continents, Geology, 38, 131–134, https://doi.org/10.1130/G30461.1, 2010.

Stegman, D. R., Farrington, R., Capitanio, F. A., and Schellart, W. P.: A regime diagram for subduction styles from 3-D numerical models of free subduction, Tectonophysics, 483, 29–45, https://doi.org/10.1016/J.TECTO.2009.08.041, 2010.

Thielicke, W. and Stamhuis, E. J.: PIVlab – Towards User-friendly, Affordable and Accurate Digital Particle Image Velocimetry in MATLAB, Journal of Open Research Software, 2, https://doi.org/10.5334/JORS.BL, 2014.

van Dinther, Y., Morra, G., Funiciello, F., and Faccenna, C.: Role of the overriding plate in the subduction process: Insights from numerical models, Tectonophysics, 484, 74–86, https://doi.org/10.1016/J.TECTO.2009.08.038, 2010.

Van Dinther, Y., Morra, G., Funiciello, F., Rossetti, F., and Faccenna, C.: Exhumation and subduction erosion in orogenic wedges: Insights from numerical models, Geochemistry, Geophysics, Geosystems, 13, https://doi.org/10.1029/2011GC004011, 2012.

van Keken, P. E. and Wilson, C. R.: An introductory review of the thermal structure of subduction zones: I—motivation and selected examples, Progress in Earth and Planetary Science 2023 10:1, 10, 1–20, https://doi.org/10.1186/S40645-023-00573-Z, 2023.

von Huene, R. and Scholl, D. W.: Observations at convergent margins concerning sediment subduction, subduction erosion, and the growth of continental crust, Reviews of Geophysics, 29, 279–316, https://doi.org/10.1029/91RG00969, 1991.

Wada, I., Wang, K., Wada, I., and Wang, K.: Common depth of slab-mantle decoupling: Reconciling diversity and uniformity of subduction zones, Geochemistry, Geophysics, Geosystems, 10, 10 009, https://doi.org/10.1029/2009GC002570, 2009.

Wang, Y., Zhang, L.-F., Li, Z.-H., Li, Q.-Y., and Bader, T.: The exhumation of subducted oceanic-derived eclogites: Insights from phase equilibrium and thermomechanical modeling, Tectonics, 38, 1764–1797, 2019.

Warren, C. J.: Exhumation of (ultra-)high-pressure terranes: Concepts and mechanisms, Solid Earth, 4, 75–92, https://doi.org/10.5194/SE-4-75-2013, 2013.

Weijermars, R.: Flow behaviour and physical chemistry of bouncing putties and related polymers in view of tectonic laboratory applications, Tectonophysics, 124, 325–358, https://doi.org/10.1016/0040-1951(86)90208-8, 1986.

Willett, S., Beaumont, C., and Fullsack, P.: Mechanical model for the tectonics of doubly vergent compressional orogens, Geology, 21, 371–374, 1993.

Xue, K., Schellart, W. P., and Strak, V.: Overriding Plate Deformation and Topography During Slab Rollback and Slab Rollover: Insights From Subduction Experiments, Tectonics, 41, e2021TC007 089, https://doi.org/10.1029/2021TC007089, 2022.

Yamato, P., Agard, P., Burov, E., Le Pourhiet, L., Jolivet, L., and Tiberi, C.: Burial and exhumation in a subduction wedge: Mutual constraints from thermomechanical modeling and natural P-T-t data (Schistes Lustrés, western Alps), Journal of Geophysical Research: Solid Earth, 112, https://doi.org/10.1029/2006JB004441, 2007.